1992

Improvement of Reliability of Conpressors for Domestic Refrigerators Using HFC134a

T. Iizuka
Hitachi

R. Naka
Hitachi

H. Hata
Hitachi

M. Gommori
Hitachi

A. Ishiyama
Hitachi

See next page for additional authors

Authors
T. Iizuka, R. Naka, H. Hata, M. Gommori, A. Ishiyama, and Y. Homma

IMPROVED CHARACTERISTICS OF STAINLESS COMPRESSOR VALVE STEEL

Sören Olsson
Research and Development Centre
AB Sandvik Steel
S-811 81 Sandviken, Sweden

ABSTRACT

The conclusions of an experimental program involving altered tensile strength and microstructure of stainless compressor valve steel are described. The paper presents the results of measurements of ductility, corrosion resistance, bending fatigue strength and damping. Encouraging indications have been achieved concerning the possibilities to further improve the characteristics of current material.

1 INTRODUCTION

One of the essential properties of a compressor valve steel is its ability to resist the stresses, created by the repeated bending of the valve without fracturing. The material parameters which control this fatigue strength are in principle well known. For example, a high static strength and compressive surface stresses contribute to improved fatigue strength, while rough surfaces and corrosion have the opposite influence.

Since long, there have been two types of materials available for the manufacture of compressor valves, one being carbon steel with a composition corresponding to AISI 1095. The other is a martensitic chromium steel based on AISI 420 but with an addition of 1 % Molybdenum.

The fatigue strength of compressor valves manufactured from these steel types has probably increased by the development of

- metallurgical processes giving cleaner steels and
- valve manufacturing methods resulting in improved edge and surface properties and controlled surface stresses.

On the other hand, only marginal changes have been made concerning mechanical properties of compressor valve steels since specifications were originally set. Corrosion has been a limited problem in most compressor applications why little attention has been paid to corrosion resistance of the stainless grade.

As service conditions in the compressors currently are subject to change, partly as a result of new refrigerants and lubricants being introduced, a gradual substitution of carbon steel valves seems to take place, favouring the stainless material. In addition, compressor designers have the ambition to increase the efficiency of compressors which makes for higher mechanical load on the valves.

For the reasons indicated above it has been considered to be of interest to evaluate the potential for improved characteristics of stainless compressor valve steel. In this paper, the results of an experimental program will be discussed.

2 EXPERIMENTAL

The tested material was Sandvik 7C27Mo2. Nominal composition and specified tensile strength of this material is given in table 1.

Trial strips with thicknesses ranging between 0.152 mm (.006") and 0.508 mm (.020") were hardened and tempered to tensile strength levels above the upper limit of the currently valid specification range. The heat treatment was made in the normal production equipment. These experimental strips were characterized concerning their mechanical properties. As elevated tensile strength normally causes reduction of the ductility of a steel, extra emphasis was put on ductility measures. Some of the strips were exposed to fatigue testing. The resistance to pitting corrosion was evaluated and an attempt was made to measure the damping properties of the material. Microstructures were assessed.

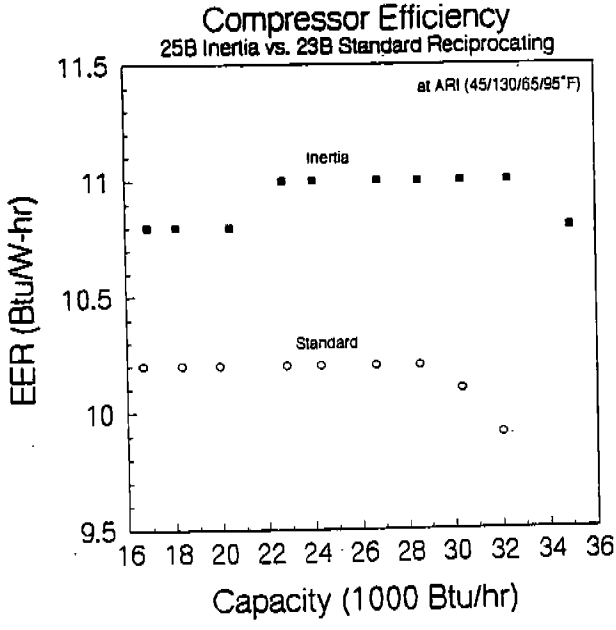

Fig. 4

H25B Life Test Summary

Test Completed	*Completed Life Tests* Number of Compressors
•Standard Slug	26
•Start/Stop	38
•High Compression	19
•Defrost Cycle	14
•Continuous Frostback	9
•High Load	26
•High Mass Flow	6
•Heat Pump	21
•Unitary Slug Test	9
•Continuous Run	2
Grand Total	170

Table 4

Temperature Profile
at ASRE/T (ARI in Parenthesis)

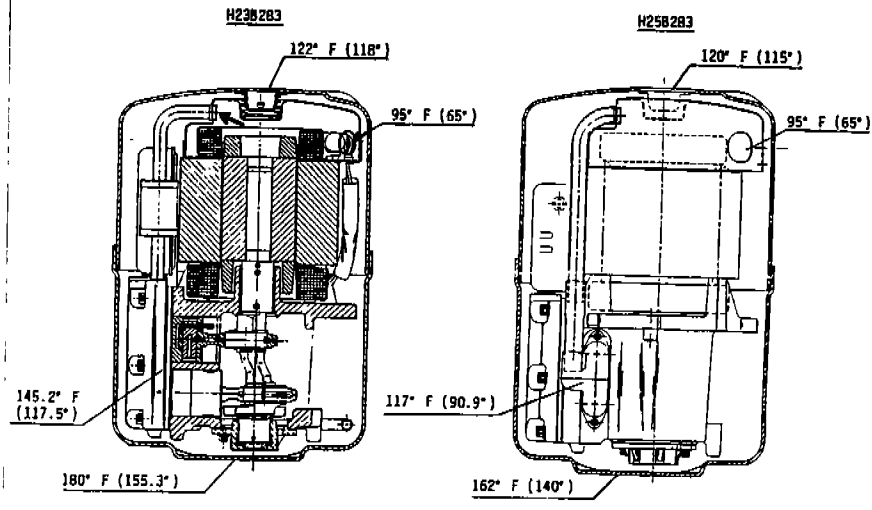

Fig. 2

Bristol Compressors

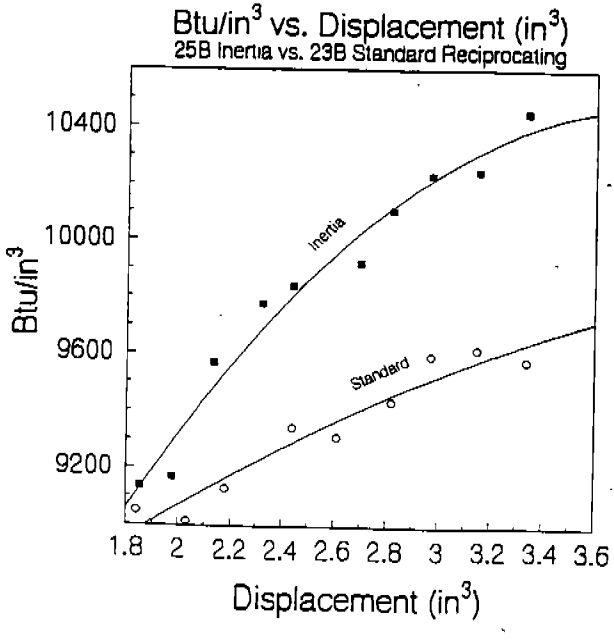

Fig. 3

Graph 2

"S/N DATA" , KADEL E-1230

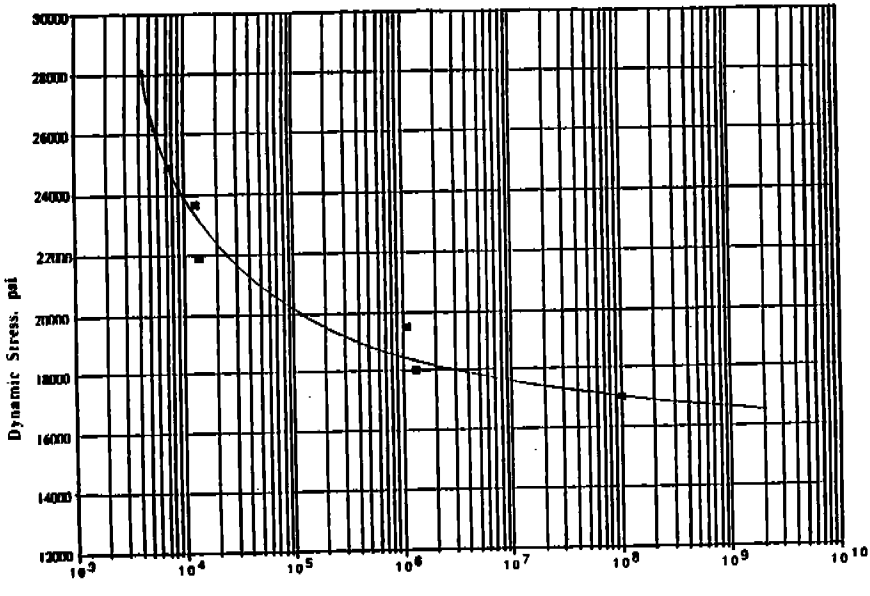

SUCTION VALVE

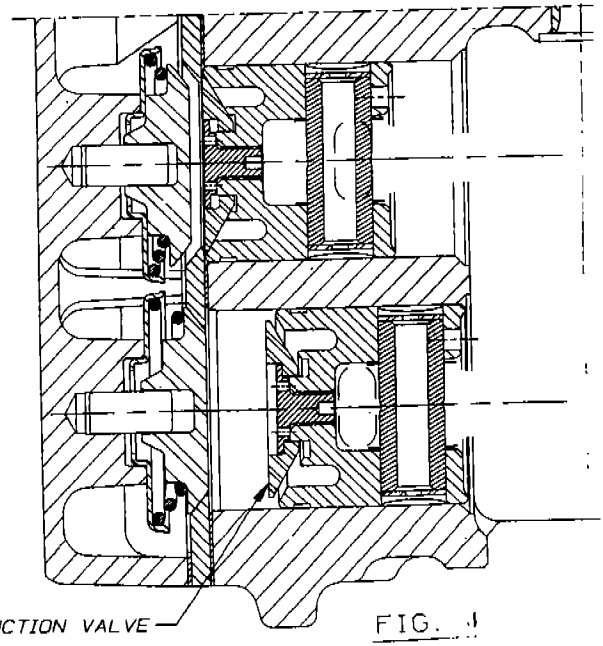

FIG. 1

TABLE 3

Fatigue Strength of Reinforced Engineering Thermoplastics

(data from 39th SPI RP/C Conference, ASTM D-671)

(Room Temperature @ 1,800 cycles/min)

MATERIAL	GLASS FIBER, %	CARBON FIBER, %	STRENGTH, PSI @10^6 CYCLES	STRENGTH, PSI @10^7 CYCLES
Nylon 6/6	--	--	3,400	3,100
Nylon 6/6	30	--	8,000	5,900
Nylon 6/6	--	30	13,000	8,000
PAEK	--	30	18,000	17,000
Polyethersulfone	30	--	16,000	5,000
Polyethersulfone	--	30	22,000	6,700
Polyphenylene Sulfide	--	30	13,000	9,500

Graph 1 shows the fatigue resistance of neat KADEL E-1000 at room temperature with the testing being done by Fatigue Dynamics using bending fatigue at ~30 Hertz.

In consideration, based on the chemistry and type of reinforcement used in KADEL E-1230, a more severe reverse bending fatigue test was conducted on this product by Fatigue Dynamics. This test has the specimen going through two opposed bends during the same cycle speed of ~30 Hertz. To enhance the testing, the data expressed by Graph 2 was conducted at 250°F, just below the Tg of the base resin which occurs at ~300°F. Testing was done at 350F using these same conditions and it was found that ~7,000 psi stress yielded <100,000 cycles to failure and that ~5,300 psi (which was the same applied strain as 7,000 psi stress at 250F) yielded ~200,000 cycles to failure.

KADEL materials demonstrate superior performance to bending fatigue. Combined with their inherent chemical resistance and superior mechanical and thermal properties, they lead the field of high performance thermoplastics for demanding industrial applications.

"S/N DATA", KADEL E-1000 neat Graph 1

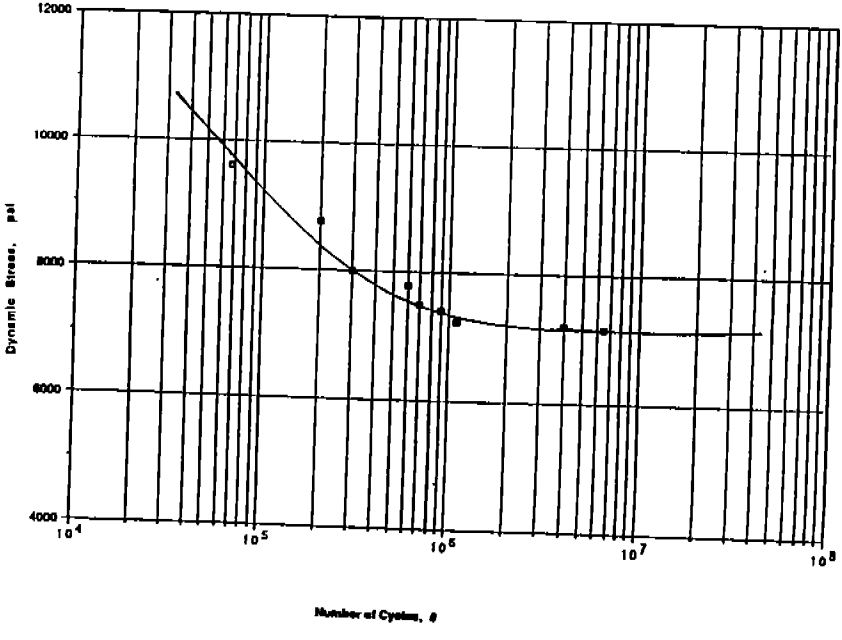

Polymer Characteristics

Characteristic	Thermid MC6000	Vespel SPI "M"	Peek 450G	Ultem 6000	Torlon 4203L	Shamban 17445	Kadel E1230
Tensile strength(psi) at 73° F	12,000	12,500	14,500	15,000	22,000	31,000	30,000
Elongation at break (%)	2	7.5	35	30	15	2	1.5
Flexural modulus (psi) at 73° F	650,000	450,000	550,000	440,000	730,000	2,600,000	2,300,000
Poisson's ratio	——	0.41	0.42	——	0.38	——	0.32
Deflection temp.(°F) at 264 psi	——	680	320	420	532	554	634
Density (lbs/in3)	0.049	0.052	0.048	0.047	0.051	0.051	0 052
Water absorption after 24 hrs.	0	0.24	0.15	0.28	0.33	0.06	0.02
Hardness	91 Shore D	45-58 RWE 92-102 RWM	——	110RWM	86RWE	110RWM	——
Fatigue endurance (psi) at 10(7) and 73°F	——	6,000	11,500	——	6,000	——	12,000
Fatigue endurance (psi) at 10(7) and 275°F	——	4,000	——	——	2,400	——	7,000
Friction coef. @ PV-25000	0.21	0.29	0.15	——	0.33	——	0.20
Izod impact : Notched Ft-lb/in: Un-notched	—— ——	1.5 30	1.6 no break	—— ——	2.7 20	1.1 11	1.5 11.2
Type Material	Polyimide	Polyimide (machined)	Polyether-etherketone	Polyethe-rimide	Polyamide-imide	Carbon re-inforced polyether-etherketone	30% carbon reinforced PAEK (polyaryl-etherketone)

Table 1

TABLE 2 Selected High-Performance Thermoplastics

GENERIC NAME	MANUFACTURER	TRADE NAME
POLYKETONES		
Polyetheretherketone (PEEK)	Imperial Chemical Industries (ICI)	Victrex PEEK
Polyetherketone (PEK)	Imperial Chemical Industries (ICI)	Victrex PEK
Polyetherketoneketone (PEKK)	E.I. Dupont de Nemours	PEKK (1)
Polyetherketoneetherketoneketone (PEKEKK)	BASF	Ultrapek
Polyketone	Amoco Performance Products	Kadel
POLYARYLENE SULFIDES		
Polyphenylene sulfide (PPS)	Phillips Petroleum Company	Ryton PPS
Polyarylene sulfide (PAS)	Phillips Petroleum Company	Ryton PAS-2 (2)
Polyphenylene sulfide sulfone (PPSS)	Phillips Petroleum Company	Ryton S PPSS (2)
POLYAMIDES		
Polyamide	E.I Dupont de Nemours	J 2 (1,2)
Polyamideimide (PAI)	Amoco Performance Products	Torlon
POLYIMIDES		
Polyarylenelmide	E.I Dupont de Nemours	K-Polymer
Polyarylenelmide	E.I Dupont de Nemours	N-Polymer
Polyimide	Ethyl Corporation	EYMYD
Polyetherimide (PEI)	General Electric Company	Ultem
Polyetherimide	American Cyanamid	Cypac
Polyketoimide	Mitsui Toatsu Chemicals Inc. (MTC)	Lare-TPI, New-TPI
Polyketoimide	Rogers Corp	Durimid

(1) Is or will be available only as custom finished composite material parts
(2) Not commercially available but nearly
(3) Not expected to be commercially available as a matrix for composite material

REFERENCES

[1] High Performance Thermoplastic Resins and their Composites, Sylvie B'eland.

[2] 39th SPIRP/C Conference, ASTM D-671.

Kadel E-1230 (Polyaryletherketone, PAEK) has proven to be the most suitable. The selected high-performance thermoplastic is shown in Table 2. Table 3 compares the strength of different polymers at room temperature. Graphs 1 and 2 depict bending fatigue of Kadel E-1000 at and reverse bending fatigue of Kadel E-1230, respectively.

Availability, pricing, design, molding, and machining are also important factors in the successful application of the suction valves (shown in Fig. 1).

Contrary to the standard practice of "Swedish Flapper Valve Steel" suction valve on a steel valve plate, the polymer suction valves simply rest on the inner and outer seats of the machined cast iron pistons. The retainer screwed into the piston post controls the lift of the suction valve which is optimized to achieve the desired efficiency and sound level of the compressor.

The suction gas is routed directly through the crankcase body into the piston suction ports. The direct gas is much cooler (Fig. 2) and has less pressure drop as it flows through the 360° opening of the suction valve. The result is higher BTU/cubic inch (Fig. 3) and higher efficiency of the pump (Fig. 4).

ENDURANCE TESTING

The different polymer valves have been evaluated to assure the efficiency of the compressor. Also extensive endurance testing of the different valves has been undertaken to select the final polymer, which is 30% carbon reinforced PAEK. Finite element analysis has been used extensively in designing the valve and correlated with the actual performance and life testing. A large database has been constructed. Life testing of Inertia compressors at the different abuse and accelerated conditions is summarized in Table 4.

CONCLUSION

Control of base material (resin pallets) and molding process (humidity, temperature control, melting, feeding, gating, and injection) must be perfected to control porosity, shrinkage, cracking, and other problems during injection molding. Machining to the final dimensioned valves is another milestone. Matching the mating parts, e.g., piston seats and valve contact areas is very critical to the performance. By perfecting these features, the polymer valve has been successfully implemented in the Inertia compressor.

ACKNOWLEDGEMENT

The authors would like to acknowledge the substantial contribution to this paper by David Gilliam and Hugh Stringer. The authors also wish to thank Bristol Compressor's upper management for their support and permission to publish this paper.

Use of Polymer Suction Valve in Piston on the Low Side Compressor

Prasanta K. Roy and Michael A. Di Flora
Bristol Compressors, Bristol, VA (U.S.A)

ABSTRACT

Although plastic utilization is abundant in the automotive industry and growing day by day, its usage is very limited, especially in the running gear of air conditioning and refrigeration compressors.

In recent years, different polymers have been developed by several manufacturers and the properties of some are suitable for use as a valve material for reciprocating compressors. In Inertia compressors, Kadel suction valves are utilized to attain high efficiency and reliability under wide range of compression ratios. For this reason, the Inertia compressor is very suitable for heat pump air conditioners.

INTRODUCTION

After the Energy Crisis, energy conservation has been the most important topic in the field of air conditioning. In the United states, the regulation of system efficiency started in 1992. Besides the governmental regulations, higher efficiencies have been required from the distributors to meet the customer's needs concerning energy savings.

In such a situation, there came a strong demand for higher efficiency compressors, because the improvement of compressor efficiency is the most economical method to increase unit efficiency in spite of technological difficulties. Thus, most compressor manufacturers have been eagerly improving conventional compressors and developing new ones.

The Inertia compressor is a new generation of reciprocating compressor, utilizing polymer suction and discharge valves.

This paper describes the properties, design, development, testing, and implementation of the polymer suction valves in the Inertia pump, which is one of the highest efficiency reciprocating compressors in the market today.

DESIGN FEATURE

The plastic valve when used dynamically in a compressor, running approximately five million cycles in 24 hours, is very critical and must have the physical and mechanical properties to withstand the cyclic loading, high temperature, impact, and fatigue. High tensile strength (30,000 psi), low elongation (1.5%), high flexural modules (2.3 million psi) and high deflection temperature (634°F) are some of the key properties of the polymer suction valve material. Table 1 shows the characteristics of different polymers that have been evaluated for the Inertia compressors.

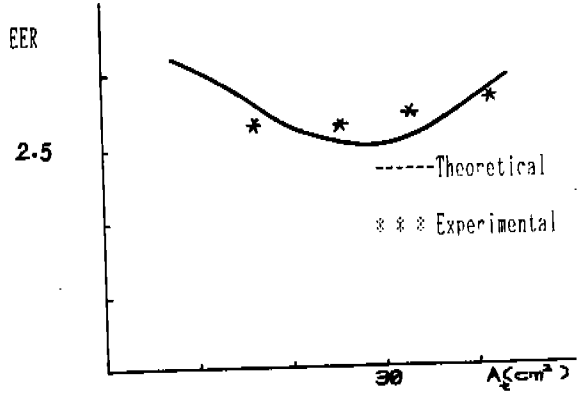

Fig.6 EER / sealing ring area diagram

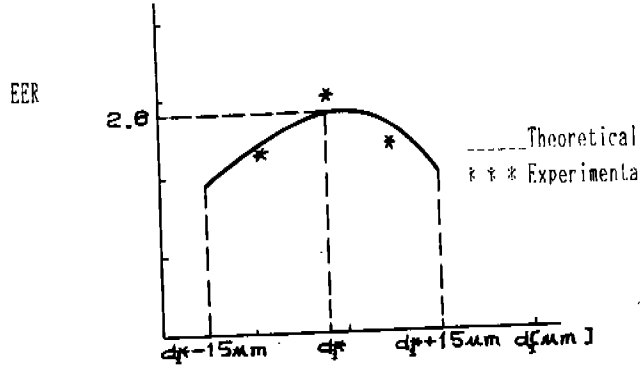

Fig.7 EER / pin diameter diagram

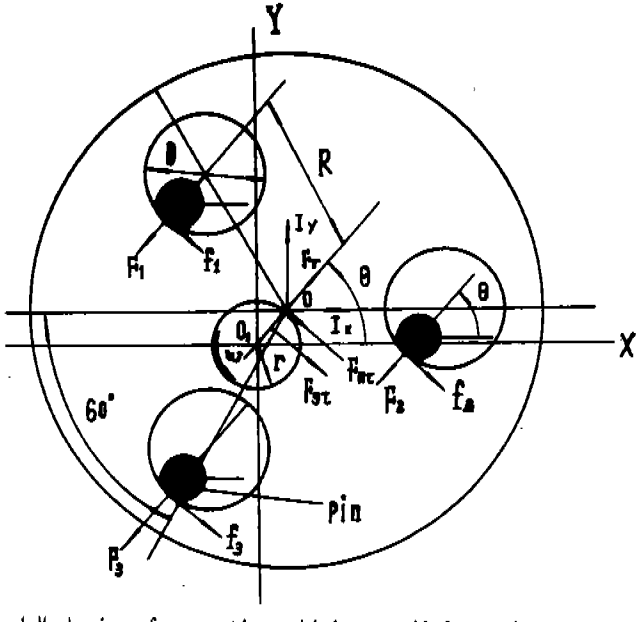

Fig.4 Mechanism of preventing orbiting scroll from self-rotation

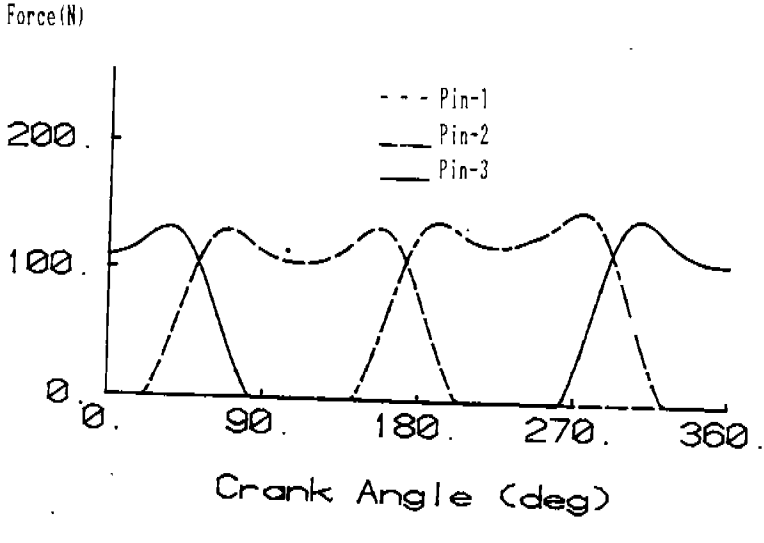

Fig.5 Force acting on 3--pins

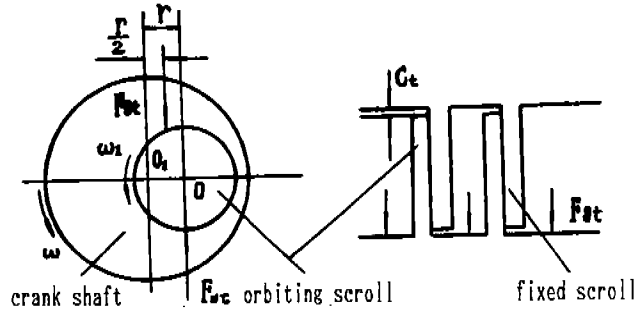

Fig.1 Gas forces acting on orbiting scroll

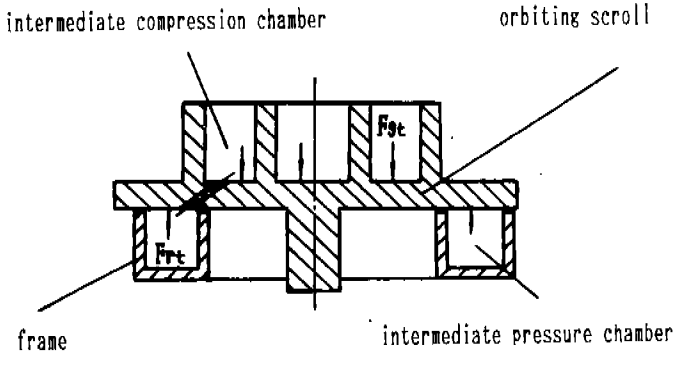

Fig.2 Balancing mechanism of intermediate pressure chamber

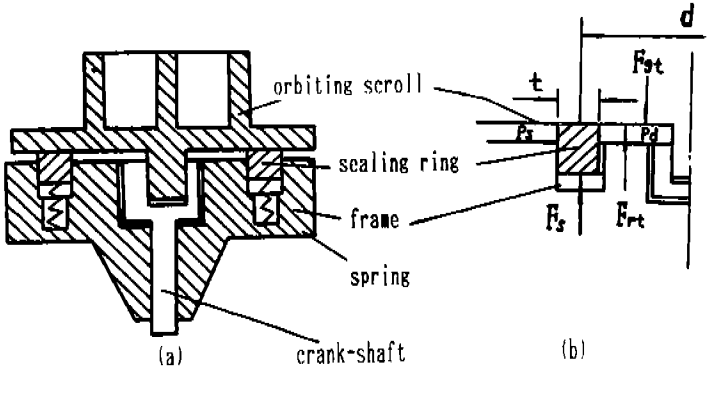

Fig.3 Balancing mechanism of axial gas force.

$M_{r\tau}$ ---self-rotation moment of orbiting scroll;

O---center of orbiting scroll;

O_1---center of fixed scroll or crank shaft;

p_s---suction pressure;

p_d---discharge pressure;

$P(\theta)$---gas pressure in intermediate pressure chamber;

r----orbiting radius;

R----distance from the center of orbiting to the center of pin hole;

t----width of sealing ring;

θ ---orbiting angle;

ω ---angular velocity of shaft;

ω_1---angular velocity of orbiting scroll self-rotation;

μ_0---coefficient of sliding friction.

REFERENCES:

[1]. Noriaki Ishii, "A STUDY ON DYNAMIC BEHAVIOR OF A SCROLL COMPRESSOR ", Proc. of 1986 ICEC (PURDUE)

[2]. Liansheng Li, Yongzhang Yu "THE THEORETICAL ANALYSIS AND EXPERIMENTAL RESEARCH FOR A REFRIGERATING SCROLL COMPRESSOR", Proc. of 1990 ICEC (PURDUE)

[3]. James W.Bush, "SCROLL COMPRESSOR DESIGN CRITERIA FOR RESIDENTIAL AIR CONDITIONING AND HEAT PUMP APPLICATIONS", Proc. of 1988 (PURDUE)

CONCLUSIONS

1. Axial and tangential gas forces acting on the orbiting scroll have been analysed. These two forces will influence efficiency and reliability of the compressor, it must be balanced perfectly.

2. Using discharge pressure in a sealing ring is a easy way to balance the axial force and a optimizing diameter of the ring is found by calculation and experiment.

3. The self-rotation of orbiting scroll may be prevented by the pin mechanism and the analysis of the acting forces on the pins has been carried out.

SYMBOLS

A_1---theacting area of intermediate pressure chamber on the orbiting scroll;

A_c---the acting area of oil in the sealing ring;

C_t---axial clearance;

d ---the intermediate diameter of sealing;

d_1---pin diameter;

D ---pin hole diameter (D=d1 + 2 * r);

EER---energy efficiency ratio;

f_1, f_2, f_3---friction force between orbiting scroll and pins;

F_1, F_2, F_3---the acting forces between pins and orbiting scroll;

F_{gt}---axial gas force acting on orbiting scroll;

$F_{g\tau}$ ---tangential gas force acting on orbiting scroll;

FN_τ ---pushed force of crank shaft;

F_r---radial gas force acting on orbiting scroll;

F_{rt}---pushed force of axial direction;

F_s---spring force;

I_x, I_y---inertial force of orbiting scroll;

M_s---mass of orbiting scroll;

or the orbiting scroll. The balancing equtions of forces acting on the orbiting scroll are represented as follows:

In X axis,

$$I_x + F_r * \cos(\theta) + (f_1+f_2+f_3) * \sin(\theta) - (F_1+F_2+F_3) * \cos(\theta) = 0. \quad (4)$$

In Y axis,

$$I_y + F_r * \sin(\theta) + (f_1+f_2+f_3) * \cos(\theta) - (F_1+F_2+F_3) * \sin(\theta) = 0. \quad (5)$$

The movement about point O is

$$-F_{rt} * r/2 - F_1 * R * \sin(120^\circ - \theta) - f_1 * [R * \cos(120^\circ - \theta - D/2) + F_2 * R \sin(\theta)$$

$$+ f_2 * (R * \cos(\theta) - D/2) + F_3 * R * \sin(60^\circ - \theta) - f_3 * [R * \cos(60^\circ - \theta) + D/2] = 0. \quad (6)$$

EXPERIMENT AND RESULLTS ANALYSIS

The thermodyamic model and computer program of scroll compressor working process [2] are directly applied to the calculation of computer.

A prototype of scroll compressor for air condition has been developed by authors, which is consisted of the anti-self-rotation mechanism using three pins and the axial gas force balancing mechanism using oil in discharge pressure in a sealing ring. The refrigeration quantity of compressor is 10,000 Kcal/h.

The results of theoretical calculation and experimental test are shown in Fig.6 and Fig.7. Fig.6 represents the relation between EER and A_t, Fig.7 represents the relation between EER and d_1.

Under the fixed testing conditions that include the compressor working condition and the surrounding condition, because F_{rt} varies with the change of sealing ring diameter, i.e,the acting area of oil against the orbiting scroll, the input power or the volumetric efficiency of compressor will change at the same time. According to this, at a certain A_t^*, there will be a maximum EER,because when A_t is greater than A_t^*, input power of compressor increases; while the A_t is less than A_t^*, the axial clearance enlarges,and the volumetric efficiency decreases. The above two cases all makes the EER of scroll copressor decrease.

In Fig.7, there is also a maximum EER which is acquired at a certain d_1^*,the cause is that when d_1 is greater than d_1^*,the friction between tangential walls of orbiting and fixed scroll increase, the input power of compressor increases and the EER decreases; when d_1 is less than d_1^*, the orbiting scroll has a little self-rotation, the tangential gas leakage of scroll compressor enhances,and the volumetric efficiency and the EER decreases.

BALANCING MECHANISM OF AXIAL GAS FORCE

The axial gas force acting on orbiting scroll should be balanced so that the normal gas compression can be completed.Balancing gas force can be accomplished by intermediate pressure chamber or with discharge gas pressure.

Intermediate Pressure Chamber

The intermediate pressure chamber used for balancing the axial gas force acting on the orbiting scroll is shown in Fig.2.It is established on the back of orbiting scroll and connected to the intermediate sealed compression chamber through a small apeture on the orbiting scroll plate. In this case, the gas pressures in the intermediate compression chamber and the intermediate balancing chamber are equal and change with the rotation angle θ of crank shaft.

The balancing equation of axial gas force is represented by:

$$F_{rt} = P(\theta) * A1$$

$$F_{rt} - F_{gt} > 0. \qquad (2)$$

or

$$F_{rt} = 1.05 \sim 1.1\ F_{gt}$$

When orbiting scroll moves, the gas in the intermediate chamber leaks to the suction pressure side and the seal of this kind of leakage is more difficult.

The Gas In Discharge Pressure

The axial gas force balance is also completed by using the balancing mechanism of gas discharge pressure, which is consisted of a sealing ring and put in the frame, as shown in Fig.3 a), Fig.3b) shows the relation of forces. The balance relation of force is :

$$F_{rt} = F_s + \pi\ d * t * p_d$$

$$F_{rt} - F_{gt} > 0. \qquad (3)$$

Owing to the oil in discharge pressure being exerted directly on the sealing ring, the gas leakage through the sealing ring will be very little. It should be pointed out that the liquid collision and overload of scroll compressor need a special adjusting mechanism of orbiting radius.

BALANCING MECHANISM OF SELF-ROTATION MOVEMENT

The three pins mechanism used to prevent the orbiting scroll from self-rotation is showen in Fig.4. The one end of pins is put to the orbiting scroll or frame, the other are put into the holes in the frame

THE MECHANICAL ANALYSIS OF A SCROLL COMPRESSOR

Yongzhang Yu , Yuhua Xu , Liansheng Li
(XI'AN JIAOTONG UNIVERSITY, P.R.CHINA)

ABSTRACT

Based on thermodynamic and mechanical models, the axial and tangential forces acting on the orbiting scroll and their balance methods are discussed in this paper. Besides, a detailed analysis of orbiting mechanism of three pins is carried out too.

INTRODUCTION

The advantageous characteristics of scroll compressor have been proved in theory and experiment[1] [3] in recent years. Remarking the main influences of the axial and tangential forces acting on orbiting scroll on the performance and reliability, this paper puts forward a new balancing method and compares it with the balance means used. The mathematical model and computer program of scroll compressor working process[2] are applied to the calculation of this paper.A prototype of scroll for air condition has been developed and tested by authors. The calculated results and experimental results are consistent

THE AXIAL AND TANGENTIAL GAS FORCES ACTING ON ORBITING SCROLL

With crank shaft rotation, the center of orbiting scroll is pushed around the center of fixed scroll or crank shaft. As the gas in the sealed volumetric chambers, which are composed of the orbiting and fixed scroll,is compressed, the gas pressure increases and the orbiting scroll is forced. With the thermodyamic mathmatic model[2] and the mechanical model, the gas force exerting model is shown in Fig.1. In Fig.1 a), because the pushing force $F_{N\tau}$ of crank shaft and the tangential gas force $F_{g\tau}$ are not acted on the same point, thus makes the orbiting scroll rotate in itsself, the normal compression chambers are interfered, self-rotation moment is given by

$$M_{r\tau} = F_{g\tau} * r/2 \qquad (1)$$

In terms of Fig.1 b),the axial gas force F_{gz} acting on the orbiting scroll makes the orbiting scroll departure the fixed scroll, increasing the axial clearance C_z,and resulting in apparent decrease of volumetric efficiency.

CONCLUSIONS

A program for obtaining the overall load performance of main and sub bearings in a scroll compressor was developed, and the analytical method of this program was applied to a small capacity model in this paper. The following conclusions as regards the basic bearing characteristics and bearing design guidelines can be drawn from the results.

(1) While operating between 15 and 120 Hz, at approximately 75 Hz or less an edge reaction force occurs in the main bearing, and the percentage of the combined reaction force accounted for by this edge reaction force increases as the frequency decreases. Also, the sub bearing constantly maintains a state of hydrodynamic lubrication.

(2) Discrepancy affects both main and sub bearing performance, and as the relative angle of discrepancy to the direction of the gas load changes, the eccentricity ratio of both bearings changes. Inclination, however, has virtually no effect on main bearing performance, and only changes the eccentricity ratio of the sub bearing.

(3) In order to evaluate the advance of shaft wear in the main bearing, the tolerance limit F·V value obtained from wear tests needs to be plotted on the F·V chart obtained in this study. The oil viscosity and discrepancy tolerance should be set so that the F·V value of the compressor under actual operating conditions is within these tolerance limits.

(4) The factor restricting inclination is the occurrence of metallic contact in the sub bearing at 15 Hz and 120 Hz, and the inclination tolerance limits are shown in the tolerances graph in this report.

(5) The clearance ratio should preferably be within the range 1/1000 ~ 1.5/1000, but this range may be slightly greater because the squeeze film effect of the oil film was not considered in this study.

REFERENCES

(1) Morishita, et al., Scroll Compressor Analytical Model, Proceedings of the 1984 International Compressor Engineering Conference at Purdue (1984), 487.

(2) Lane, Laub, Designing for Cantilevered Bearing Loads: Approach to Scroll Design, Proceedings of the 1988 International Compressor Engineering Conference at Purdue (1988), 1.

(3) Nieter, DeBlois, Counterweighting Scroll Compressor for Minimal Bearing Loads, Proceedings of the 1988 International Compressor Engineering Conference at Purdue (1988), 175.

contact in the sub bearing, which is then subject to extreme wear and even seizure.

The discrepancy and inclination limits under normal air conditioner operating conditions at a 3 x 10^{-3} Pa·s viscosity are shown in Figs. 12 and 13 for 15 Hz and 120 Hz, respectively. The relative angle of the direction of discrepancy to the direction of the inclination can be either detrimental (the discrepancy aggravates the inclination) or beneficial (the discrepancy attenuates the inclination) to the bearing. Both Figs. 12 and 13 illustrate the former (detrimental) case. In this case, the tolerance limit of the inclination decreases with an increase in the discrepancy, becoming a straight line rising to the left. This is because a 10 μm discrepancy is geometrically equivalent to an inclination of 8 x 10^{-5} rad.

Note that the tolerance limits (horizontal axis) for discrepancy shown by the three straight lines in Figs. 12 and 13 are the theoretical values for the change in the discrepancy tolerance at a clearance ratio of 1/1000 and 2/1000, assuming a reference discrepancy tolerance of 20 μm at a 1.5/1000 clearance ratio. Precise actual values must be obtained experimentally.

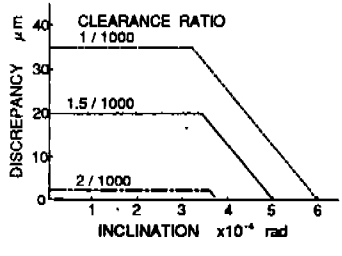

Fig. 12 Discrepancy and inclination tolerance limits(1) (15Hz)

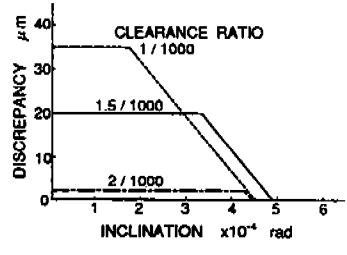

Fig. 13 Discrepancy and inclination tolerance limits(2) (120Hz)

(3) Selecting the clearance ratio

Judging from Fig. 10, it is preferable to keep the clearance ratio as close to 1/1000 as possible in order to keep the F_{max}·V value small. In addition, it is clear from the discrepancy and inclination tolerance limit graph at 15 Hz (Fig. 12) that a clearance ratio of 1/1000 is best for increasing tolerance. In the discrepancy and inclination tolerance limit graph at 120 Hz (Fig. 13), however, a clearance ratio of 1.5/1000 provides the greatest tolerance to inclination. Therefore, if a certain amount of latitude is allowed in the clearance ratio considering the machine tolerance and ease of equipment assembly, it is preferable to keep this within the range 1/1000 to 1.5/1000.

It should also be noted, however, that this analysis does not consider the squeeze film effect of the oil film, and the optimum bearing clearance ratio might actually be greater than this because the load carrying capacity of the oil film has been slightly underestimated.

that the F_{max}·V value is within these tolerances for the intended operating conditions.

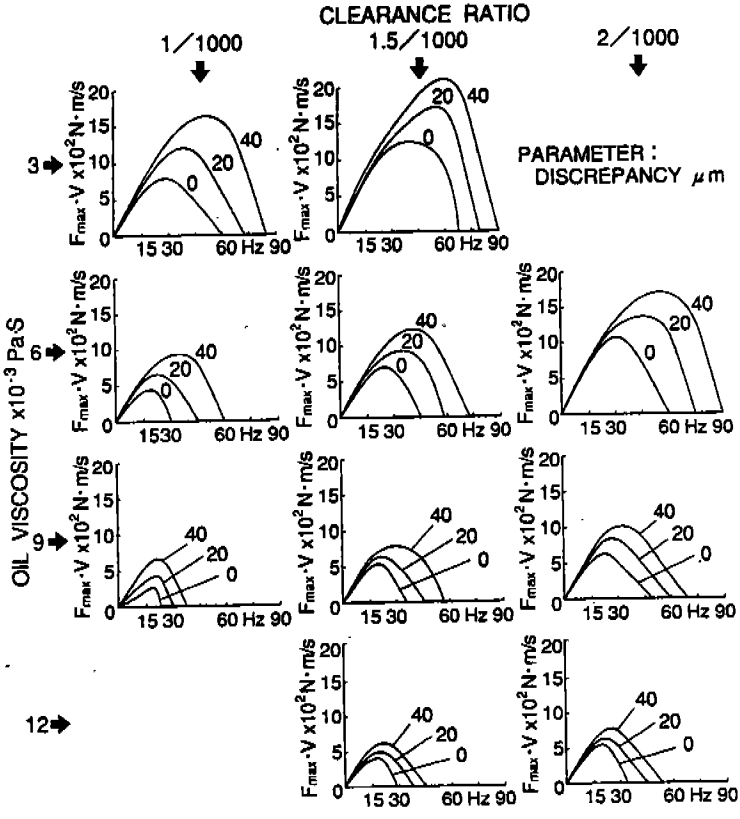

Fig. 10 F_{max}·V values for the main bearing

(2) Tolerance limits for inclination

The limiting factors for sub bearing inclination are shown in Fig. 11. One of these is the occurrence of metallic contact in the sub bearing at 15 Hz. Because metallic contact also occurs in the main bearing at this time, there is the possibility that the main shaft will stop turning. Another factor is the occurrence of metallic contact in the sub bearing at 120 Hz. If the stiffness of the subframe supporting the sub bearing is high, elastic deformation of the subframe cannot be expected to avoid metallic

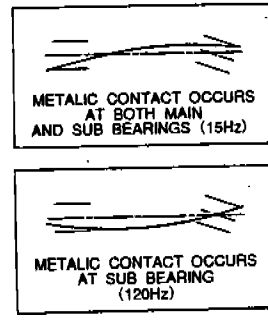

Fig. 11 Limiting factors for sub bearing inclination

(3) Determination of the optimum bearing clearance ratio

We therefore prepared several graphs based on the basic characteristics described in the previous section to study the above items.

(1) Evaluations using load and velocity

The edge load on the main bearing will increase wear of the main shaft. In general, the amount of wear W can be defined by the equations

$$W = w \cdot F \cdot l = w \cdot F \cdot V \cdot T$$

where:

w: specific wear amount (m^3/Nm)
F: load (N)
l: total sliding distance (m)
V: sliding velocity (m/s)
T: total sliding time (s)

If the specific wear amount w is assumed to be constant, the parameter by which the amount of wear W in a given time T can be compared is the product of the load F and the sliding velocity V (F·V). If the edge reaction force and circumferential velocity are used as F and V, respectively, the product F·V can be used to evaluate the performance of the main bearing under an edge reaction force. Note that if there is any discrepancy, the magnitude of the edge reaction force will vary according to the angle of the discrepancy, but the complications of this added parameter are avoided here by using the maximum edge reaction force F_{max} as an index for evaluation of the product F_{max}·V.

The F_{max}·V values for the main bearing when the clearance ratio and oil viscosity were changed to 1/1000, 1.5/1000 and 2/1000, and to 3, 6, 9 and 12 x 10^{-3} Pa·s, respectively, to simulate conceivable standard loads are shown in Fig. 10. The parameter used here is the amount of discrepancy, and as this value increases the F_{max}·V value also naturally increases.

The F_{max}·V value also decreases as the clearance ratio decreases. This is because the load carrying capacity of the oil film is increased by reducing the clearance ratio when the shaft is inclined to the axis of the main bearing. In addition, the load carrying capacity of the oil film increases when the viscosity is increased and the F_{max}·V value decreases. In either case, the maximum F_{max}·V value decreases and the frequency at which the F_{max}·V value becomes 0 decreases. In other words, we can see from the figure that both the peak height and width decrease.

To use this F_{max}·V value figure to evaluate main shaft wear and define the tolerance for discrepancy, it is necessary to plot the data from wear tests over the graph. Specifically, by measuring main shaft wear under a varying clearance ratio, viscosity, discrepancy, frequency, and other conditions to determine the suitability of these conditions, and plotting plural good and bad points on the F_{max}·V value graph, it is possible to obtain the F_{max}·V values of the tolerance limits. Thereafter, the designer simply needs to select the oil viscosity and discrepancy tolerances so

side of the main bearing when the direction of discrepancy is between 90° and 225°. These conditions are most severe at 90°, at which the eccentricity ratio of the upper end is 0.99. Unlike at 15 Hz, however, the eccentricity ratio of the lower end is normally high in the sub bearing, and a constant hydrodynamic lubrication state is maintained because there is excess load carrying capacity at high speeds.

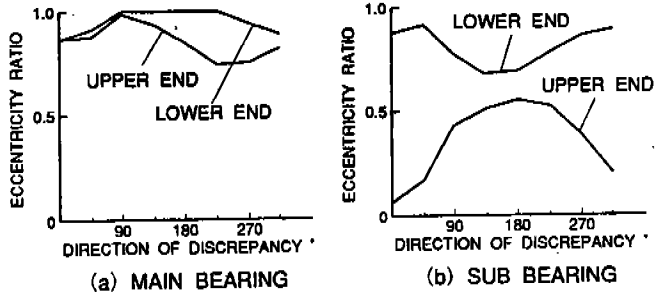

Fig. 8 Calculated bearing performance(1) (30μm discrepancy, 120Hz)

The calculated bearing performance for a 4 x 10^{-4} rad inclination at 120 Hz is similarly shown in Fig. 9. As at 15 Hz, there is virtually no change in main bearing performance even though there is a change in the direction of discrepancy. On the other hand, the eccentricity ratio of the lower end of the sub bearing is high, as described above. When the direction of discrepancy is 0° and 315°, the eccentricity ratio is 0.95, which means that metallic contact almost occurs.

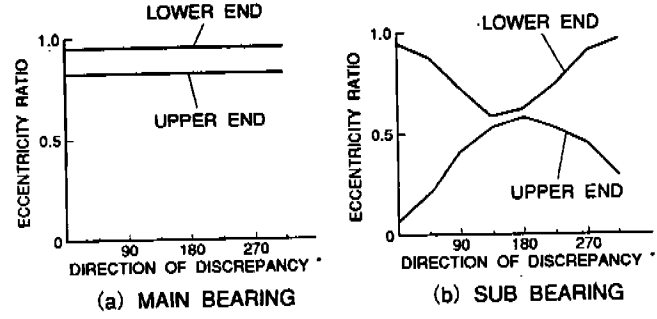

Fig. 9 Calculated bearing performance(2) (4×10^{-4} rad inclination, 120Hz)

DESIGN GUIDELINES FOR MAIN AND SUB BEARINGS

It is necessary to clarify the following three items in the design of main and sub bearings for a scroll compressor.

(1) Determination of the limits and evaluation of the absolute values of the contact force caused by edge load on the main bearing

(2) Determination of the tolerances for misalignment of the main and sub bearings

direction of the gas load changes, the eccentricity ratio of the main and sub bearings fluctuates. While there always exists the edge reaction force in the main bearing, the magnitude of the oil film reaction force is greatest (270 N) when the direction of discrepancy is 270°, and is least (84.1 N) at 90°. This is because the discrepancy acts to alleviate the inclination of the shaft inside the main bearing in the former case, but has the reverse effect in the latter case. On the other hand, while there is a slight fluctuation in the eccentricity ratio of the sub bearing compared with when there is no discrepancy (0.68 and 0.73 on the upper and lower ends, respectively), it is in a constant state of hydrodynamic lubrication.

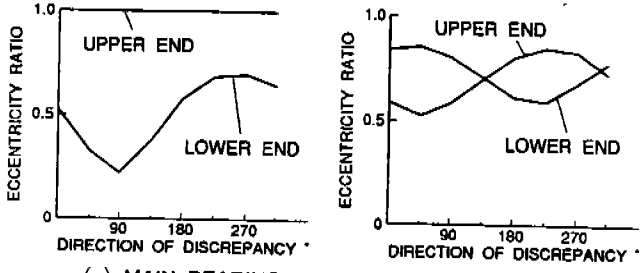

Fig. 6 Calculated bearing performance(1) (30μm discrepancy, 15Hz)

The calculated bearing performance for a 4 x 10^{-4} rad inclination at 15 Hz is shown in Fig. 7. There is virtually no change in main bearing performance even though the relative angle between the direction of the discrepancy and the direction of the gas load changes. In other words, the discrepancy of the sub bearing has virtually no effect on the main bearing. On the other hand, the eccentricity ratio of the sub bearing varies greatly with the direction of inclination, and becomes rather severe at the lower end at 45° and at the upper end at 225°.

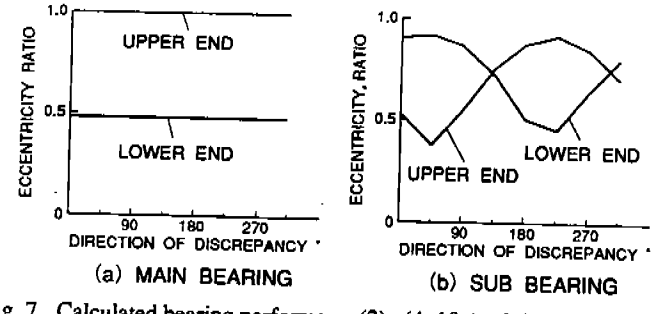

Fig. 7 Calculated bearing performance(2) (4×10⁻⁴ rad inclination, 15Hz)

The calculated bearing performance for a 30 μm discrepancy at 120 Hz is shown in Fig. 8. Because the centrifugal load 1 is 1000 N at 120 Hz, greater than the gas load of 745 N, the operating conditions of the main bearing become extreme at the lower end (the rotor end). As a result, the shaft strongly contacts the lower

reaction forces of the main bearing and the oil film reaction force of the sub bearing increase in a corresponding manner.

It can be seen from this figure that the oil film reaction force of the main bearing is insufficient at less than 75 Hz, resulting in an edge reaction force, and that the percentage of the combined reaction force accounted for by the edge reaction force increases as the frequency decreases. In other words, the edge reaction force accounts for more than 80% of the combined reaction force at 15 Hz, and the oil film reaction force accounts for less than 20% of the total—an extreme operating condition. Furthermore, when the reaction forces of the main and sub bearings are compared it is found that the contribution of the sub bearing is less than that of the main bearing, and that this tendency is even more pronounced at lower frequencies. Thus, when the loads act outside the bearing span, the operating conditions of the bearing (main bearing) nearest the load become even more extreme.

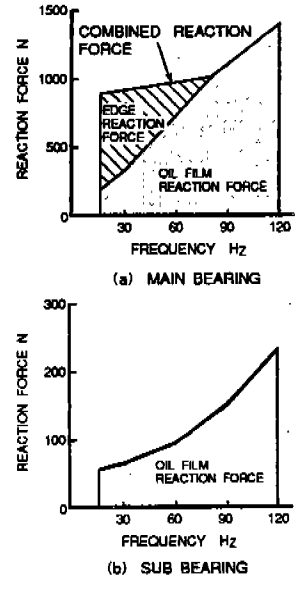

Fig. 3 Basic performance of the main and sub bearings

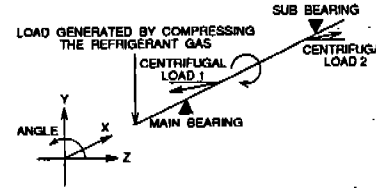

Fig. 4 Relationship between the positions of the loads acting on the main shaft

(2) Affect of misalignment

Bearing performance was computed for those cases in which there is an offset (or "discrepancy") between the center axes of the main and sub bearings, and in which the axis of the sub bearing is at an angle (or "inclination") to the axis of the main bearing. The definitions for this discrepancy and inclination are shown in Fig 5.

The calculated bearing performance for a 30 μm discrepancy at 15 Hz is shown in Fig. 6. When the relative angle between the direction of sub bearing discrepancy and the

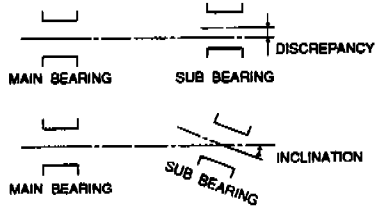

Fig. 5 Definitions for the discrepancy and inclination

(2) Reynolds' equation of incompressible Newtonian fluids can be applied to the bearing oil film.

(3) The loads acting on the main shaft are synchronous to the rotation and are of constant magnitude.

(4) Deformation of the bearings can be ignored.

From assumption (3) above, the rotating load is substituted for the static load in this analysis, and an equivalence model in which the direction of shaft rotation is reversed was used.

The first step in this analysis was to compute the deformation of the shaft by applying the finite element method using the one dimensional beam element. The eccentricity ratio of the deformed shaft in both the main and sub bearings was hypothesized, the oil film state was obtained in each bearing, and Reynolds' equation

$$\frac{1}{r^2}\frac{\partial}{\partial\theta}\left(\frac{h^3}{\mu}\frac{\partial p}{\partial\theta}\right)+\frac{\partial}{\partial x}\left(\frac{h^3}{\mu}\frac{\partial p}{\partial x}\right)=6\frac{U}{r}\frac{\partial h}{\partial\theta}$$

where:

h: oil film thickness p: hydrodynamic pressure

μ: oil viscosity U: shaft surface velocity

was applied. Reynolds' equation was then discretized using the finite element method, and the pressure distribution was obtained using the band matrix method. The base pressure (ambient pressure) at both sides of the bearings was defined as the boundary condition of the pressure, and was substituted for any pressure below this level. Because the bearing reaction force obtained from the first calculated pressure distribution does not balance in either magnitude or direction with the external forces acting on the shaft, this calculation is repeated until the magnitude and direction of the three external forces acting on the shaft and the two bearing reaction forces are balanced, by performing a convergence calculation using a Jacobi matrix.

BASIC CHARACTERISTICS OF THE MAIN AND SUB BEARINGS

Application of the analytical method described above to the scroll compressor shown in Fig. 1 is described below. Note that the diameter and bearing width of the main bearing of this compressor is 20 mm, the diameter and bearing width of the sub bearing is 16 mm, and the bearing span is 134 mm.

(1) Basic performance at selected frequencies

The basic performance of the main and sub bearings at selected frequencies from 15 ~ 120 Hz is shown in Fig. 3. The relationship between the positions of the loads acting on the main shaft is shown in Fig. 4. While the gas load is constant at 745 N, the two centrifugal loads increase with the frequency, and the combined

supported by two journal bearings flexes due to the load generated when refrigerant gas is compressed, and the action of the centrifugal force generated by the counterweights. This program was applied to a typical scroll compressor to compute the basic performance at selected frequencies, as well as the effect of misalignment of the main and sub bearing axes on bearing performance. Results showed that quantitative evaluation of the optimum bearing clearance ratio and main-sub bearing misalignment tolerance is possible.

ANALYSIS

The construction of the scroll compressor used for this analysis is shown in Fig. 1. The main shaft is supported by the main and sub bearings sandwiching the rotor, with the main bearing above and the sub bearing below. The loads acting on the main shaft include the load acting from the orbiting scroll (or "gas load"), a first centrifugal load 1 produced by the top counterweight 1, and a second centrifugal load 2 produced by the bottom counterweight 2.

Application of the gas load outside of these two bearings results in a relatively high bending moment acting to deform the main shaft. In addition, because of misalignment of the main and sub bearings resulting from assembly error, the main shaft is positioned at an angle to the axis of the main bearing. Therefore, at a low range Sommerfeld number, the oil film reaction force inside the main bearing does not provide the reaction force required in the main bearing, and the main shaft contacts the upper side of the main bearing. It was assumed in this analysis that the insufficient oil film reaction force is compensated for by the edge reaction force in this case, and the combined reaction force—the vector sum of the oil film and edge reaction forces—is the reaction force occurring in the bearing (see Fig. 2). It is therefore possible to quantitatively evaluate the contact force when metallic contact occurs.

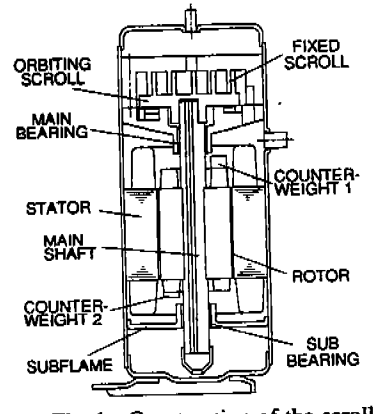

Fig. 1 Construction of the scroll compressor

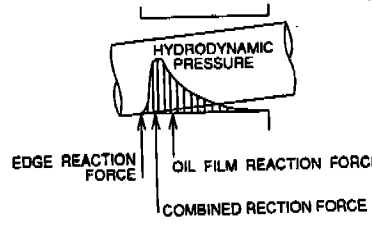

Fig. 2 Definition of the combined reaction force

The following four assumptions were also made:

(1) Deformation of the main shaft is an amount for which the beam deflection theory can be applied.

JOURNAL BEARING PERFORMANCE IN A SCROLL COMPRESSOR

Hiromu NARUMIYA*, Keiju SAKAINO**, Masahiko OIDE**

* Central Research Laboratory
Mitsubishi Electric Corporation
8-1-1 Tsukaguchi Honmachi, Amagasaki, Hyogo 661, JAPAN
Tel.: 81-6-497-7164 Fax: 81-6-497-7291
** Shizuoka Works, Mitsubishi Electric Corporation

ABSTRACT

The load carrying capacities of the main and sub bearings were obtained by mathematical analysis when a main shaft supported by two journal bearings is flexed by the action of plural loads. This analytical method was applied to a typical scroll compressor, and the basic performance of the bearings was calculated at selected frequencies. The misalignment tolerance and optimum bearing clearance ratio of the main and sub bearings were quantitatively evaluated, and meaningful guidelines for bearing design were obtained.

INTRODUCTION

High efficiency, low operating noise and low vibration characteristics have made the scroll compressor(1), together with the screw compressor, leading candidates to succeed today's reciprocating and rolling piston type compressors for many applications. A scroll compressor is typically constructed with a bearing supporting an orbiting scroll outside the two bearings supporting the main shaft. Because the load on the main shaft acts outside of the two support bearings, the load tends to bend the main shaft. In addition, the presence of assembly error in the position of these two bearings (i.e., the main and sub bearings) causes the main shaft to rotate in a twisted manner through the two bearings, so that the main bearing has to operate under extreme conditions.

The use of a roller bearing as the main bearing has been proposed as a means of reducing this twisting of the main shaft, with a ball bearing or needle bearing used for the sub bearing. As a result, there are few examples of journal bearings being used for both the main and sub bearings, and few reports in the literature regarding journal bearings other than one on experimental studies of the edge load(2) and another on ways of reducing the bearing reaction force through optimization of a counterweight.(3) There are virtually no reports about calculating the effect of bearing performance on overall scroll compressor performance with specific consideration given to the bending of a main shaft supported by journal bearings.

The authors report in this paper on the development of a program to obtain the overall load carrying capacity of the main and sub bearings when a main shaft

4) Nieter, J. J., and Barito, Tom, "Dynamics of Compliance Mechanisms for Scroll Compressors, Part I: Axial Compliance", Proceedings of the 1990 International Compressor Engineering Conference at Purdue, Vol. 1, pp. 308-316.

5) Nieter, J. J., Marchese, A. J., and DeBlois, R. L., "Dynamic Axial Compliance to Reduce Thrust Surface Friction in a Scroll Compressor", Proceedings of the 1992 International Compressor Engineering Conference at Purdue.

6) Shu, H. T., and Peracchio, A. A., "Dynamics of an Orbiting Scroll with Axial Compliance, Part 1: Simulation of Orbiter Motion", Proceedings of the 1992 International Compressor Engineering Conference at Purdue.

7) DeBlois, R. L., and Stoeffler, R. C., "Instrumentation and Data Analysis Techniques for Scroll Compressors", Proceedings of the 1988 International Compressor Engineering Conference at Purdue, Vol. 1, pp. 182-188.

8) McGovern, J. A., "Analysis of a Refrigerant Compressor Load Stand Incorporating Hot Gas Bypass and a Single Full Condensation Heat Exchanger", Proceedings of the 1984 International Compressor Engineering Conference at Purdue, Vol 1., pp. 468-477.

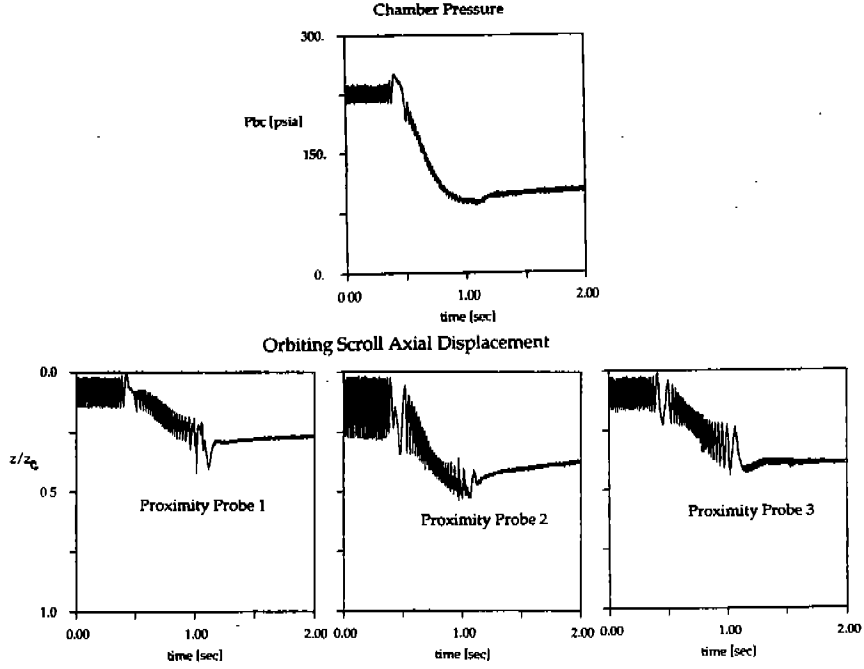

Figure 11. Compliance Chamber Pressure and Orbiting Scroll Axial Displacement at Shutdown

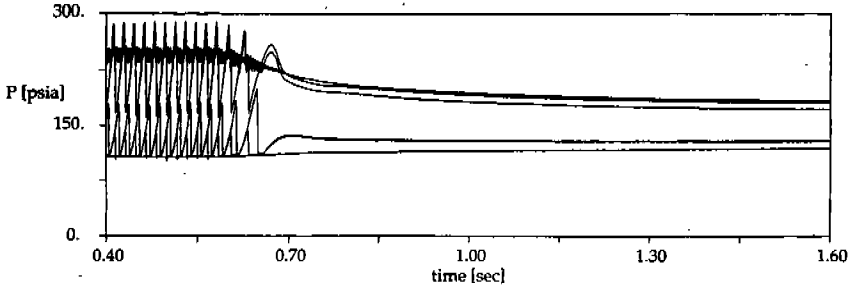

Figure 12. Compression Pocket Pressures at Shutdown with Internal Check Valve

REFERENCES

1) Inaba, Tsutomu, et al., "A Scroll Compressor with Sealing Means and Low Pressure Side Shell", Proceedings of the 1986 International Compressor Engineering Conference at Purdue, Vol. 3, pp. 887-900.

2) Tojo, Kenja, et al., "Computer model of a Scroll Compressor with Self Adjusting Back-Pressure Mechanism", Proceedings of the 1986 International Compressor Engineering Conference at Purdue, Vol 3, pp. 872-886.

3) Bush, J. W., Elson, J. P., "Scroll Compressor Design Criteria for Residential Air Conditioning and Heat Pump Applications", Proceedings of the 1988 International Compressor Engineering Conference at Purdue, Vol. 1, pp. 83-97.

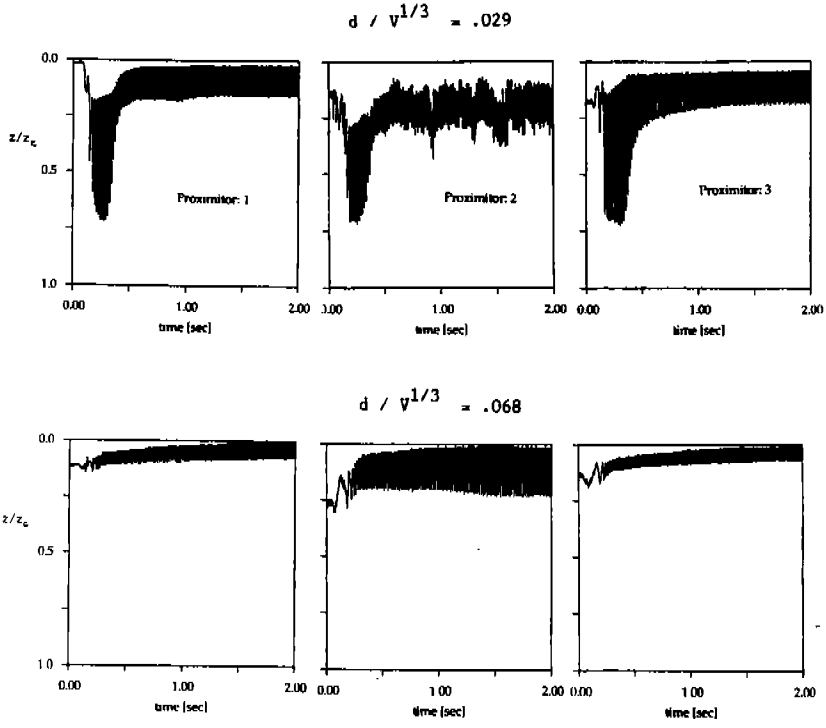

Figure 9. Orbiting Scroll Axial Displacement at Startup

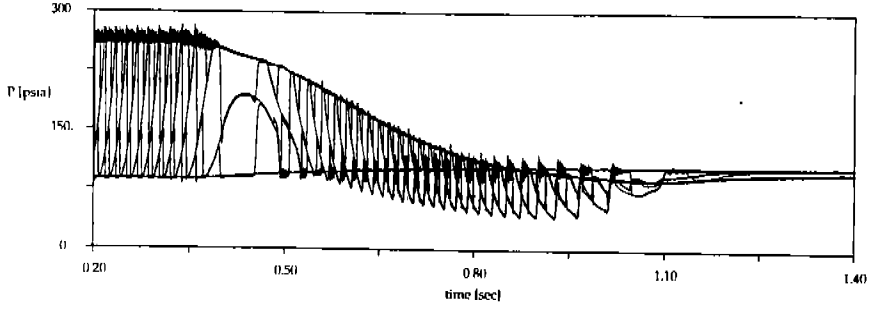

Figure 10. Compression Pocket Pressures at Shutdown

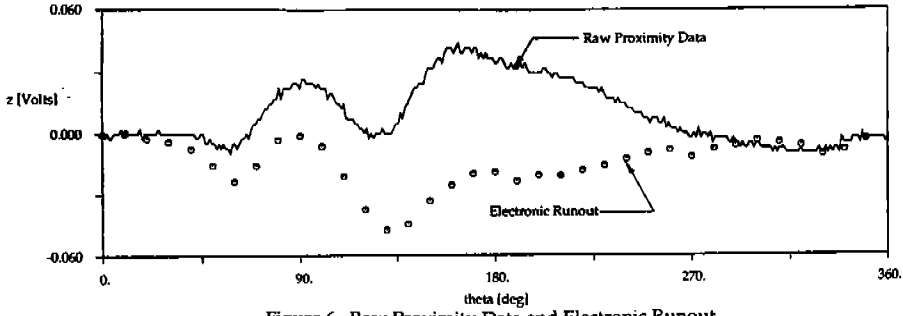

Figure 6. Raw Proximity Data and Electronic Runout

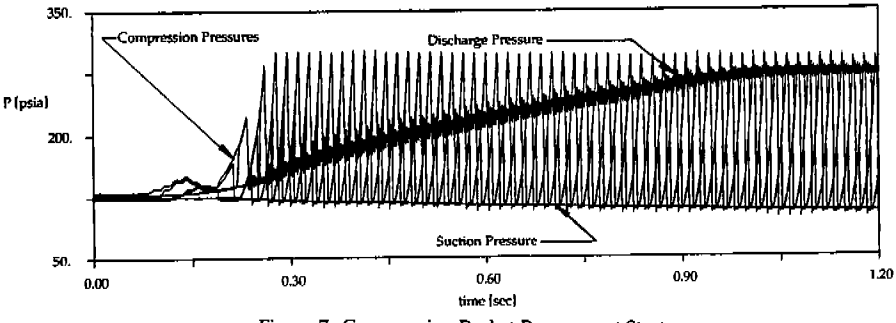

Figure 7. Compression Pocket Pressures at Startup

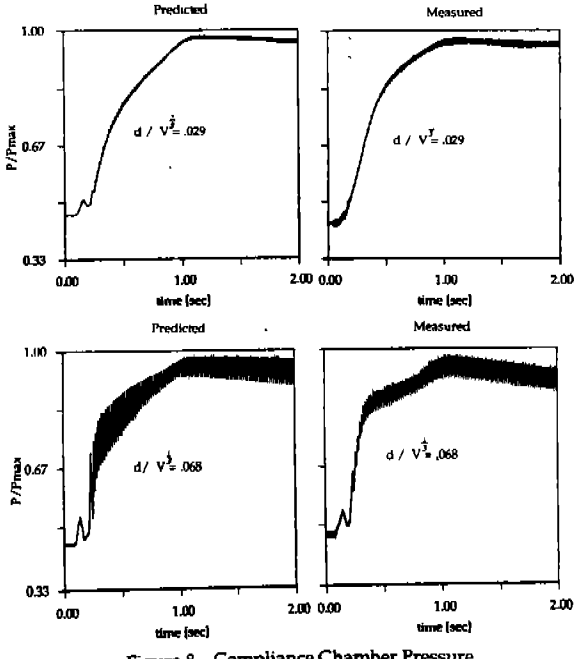

Figure 8. Compliance Chamber Pressure

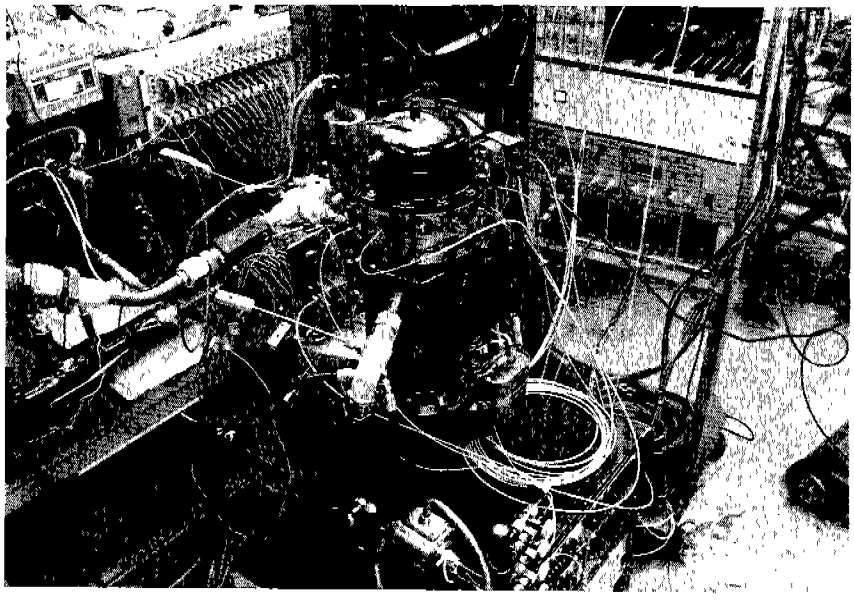

Figure 4. Laboratory Compressor in Test Configuration

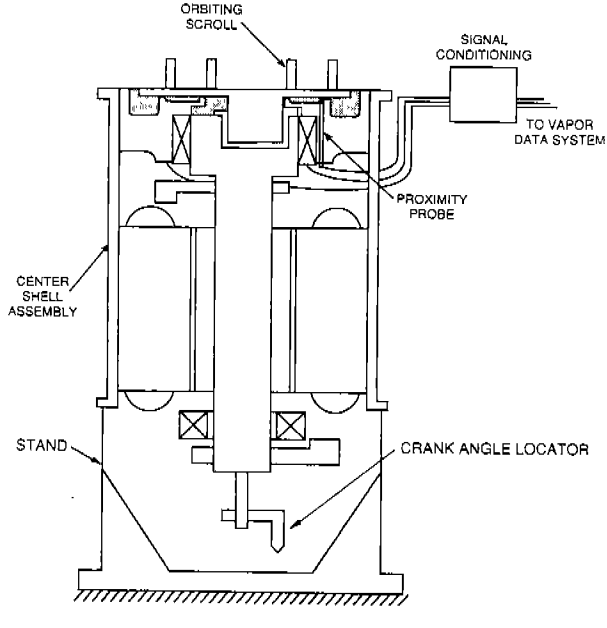

Figure 5. Determination of Proximity Probe Electronic Runout

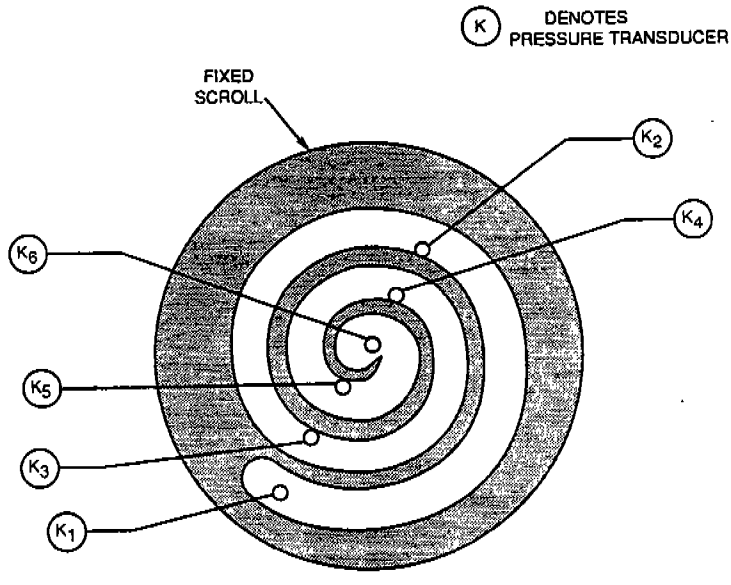

Figure 2. Compression Pocket Pressures

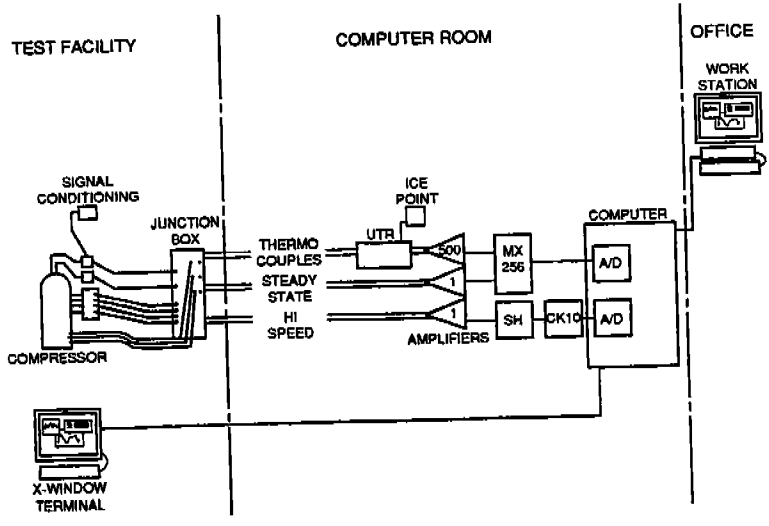

Figure 3. Data System

CONCLUSIONS

Proper design of the axial compliance mechanism can effectively minimize or even eliminate axial movement of the orbiting scroll during transient startup. Such an axial compliance mechanism will also prevent orbiting scroll axial motion during the reverse rotation encountered during compressor shutdown in scroll compressors installed with external discharge line check valves. In scroll compressors equipped with an internal check valve, little or no reverse rotation occurs at shutdown, resulting in no orbiting scroll axial motion.

Transient pressures acting on the orbiting scroll and resulting orbiting scroll axial motion can be accurately determined using appropriate instrumentation together with a state-of-the-art data system. The orbiting scroll axial vibration characteristics derived in this manner have provided a fundamental understanding of the orbiting scroll dymamics during steady state and transient operation. These experimental results will be used for validating the analytical model described in reference [6]. The experimental techniques described herein, together with continued development of the dynamic model provide a valuable tool for the scroll compressor designer.

ACKNOWLEDGMENTS

The author wishes to acknowledge the assistance of UTRC researchers Jack Shu, Ray DeBlois, Gerry Cloutier and Larry Hardin; and Tom Barito at Carrier.

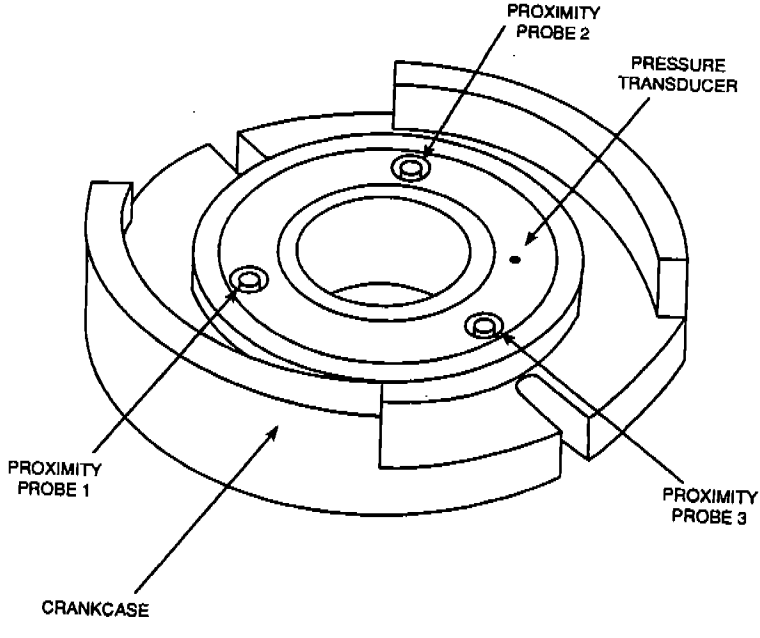

Figure 1. Proximity Probe Locations

$$\dot{m}_{sl} = \dot{m}(Pc_i, Tc_i, P_{i-1}, T_{i-1}, d_{sl}, l_{sl}, e_{sl}) \quad (1)$$

$$m_i = m_{i-1} + \dot{m}_{sl}\,\Delta t \quad (2)$$

$$\rho_i = m_i / V_{bc} \quad (3)$$

$$T_i = T_{i-1}(1 - \Delta t\,\dot{m}_{sl}/m_i) + \frac{\Delta t\,\dot{m}_{sl}}{m_i\,Cv_{i-1}}\,(h_{sl,i} + V_i^2/2) \quad (4)$$

$$P_i = P(T_i\ ,\ \rho_i). \quad (5)$$

This finite-difference analysis indicated that the transient compliance chamber pressure rise time is a function of chamber volume, supply port diameter, supply line length, and supply port location. Figure 8 is a plot of predicted and measured compliance chamber pressure for two different supply port diameters and chamber volumes. This figure shows the trade-off between transient rise time and steady state pressure pulsation. It is apparent that the larger values of $d/V^{1/3}$ (corresponding to larger line size and/or smaller compliance chamber volume) result in faster initial pressure rise and larger steady state pressure pulsations.

Figure 9 shows plots of the three proximity probe signals during transient startup conditions for the two different geometries. The normalized axial displacement z/z_c shown in these figures is the displacement of the orbiting scroll baseplate from the bottom of the fixed scroll surface divided by the total axial clearance between the fixed and orbiting scrolls. This figure indicates that the duration of orbiting scroll instability can be minimized by minimizing the compliance chamber pressure rise time.

Compressor Shutdown

In order to exaggerate the duration of reverse rotation encountered during compressor shutdown, the internal check valve was removed and replaced with a check valve in the discharge line external to the compressor. Figure 10 is a plot of compression chamber pressures during compressor shutdown for the laboratory scroll compressor in this configuration. This figure shows that when the input power was terminated, the high pressure on the discharge side of the compressor relieved through the scroll elements, causing the compressor to run in reverse. At this condition, flow reversal occurred at about 0.4 seconds causing the laboratory scroll compressor to run in reverse for about 30 shaft revolutions.

During this reverse rotation, the orbiting scroll exhibited little axial instability. This was because the compliance chamber remained sufficiently pressurized to generate upward axial forces great enough to overcome the decreasing downward axial force and overturning moment. Figure 11 shows the compliance chamber pressure and the proximity probe data during reverse rotation ($t > 0.4$ seconds).

Since the orbiting scroll exhibits little axial instability during reverse rotation, compressor shutdown does not appear to adversely effect compressor reliability. Reverse rotation does, however, result in an undesirable noise whose duration is directly related to the volume of the high pressure gas on the discharge side. Thus, one way to minimize the duration of reverse rotation is to place the check valve as close as possible to the discharge port of the scroll elements. Accordingly, the internal check valve was re-installed into the laboratory compressor directly downstream from the fixed scroll discharge port. Figure 12 is a plot of compression chamber pressures during shutdown with the internal check valve in place. This figure shows that in this configuration the laboratory scroll compressor exhibited zero reverse rotations and consequently no orbiting scroll wobble.

Test Procedure

The laboratory test compressor was integrated into a desuperheater test stand equipped with suction and discharge pressure transducers and thermocouples which enabled accurate determination of operating condition [8]. Figure 4 shows the compressor in test configuration. Prior to gathering the transient data, the compressor was operated to establish the proper valve settings to achieve the desired steady state operating condition. The compressor power was then turned off. As power was restored, instantaneous suction pressure, discharge pressure, compression pocket pressures, compliance chamber pressure, orbiting scroll baseplate proximity probe data, and crank angle reference data were acquired for the initial 2 seconds during the transient compressor startup.

The compressor was then allowed to run for approximately 2 hours until it was determined that temperatures measured in the motor, bearings, shell, and oil sump had reached steady state. Once the compressor temperatures reached steady state,. the input power to the compressor was terminated while the above pressure data and proximity data were acquired during the transient compressor shutdown.

TEST RESULTS

Proximity Probe Electronic Runout

From previous experience with high response proximity probes, it was understood that the raw output signal from each proximity probe would contain not only information related to axial displacement of the orbiting scroll baseplate, but electronic runout as well. Electronic runout is an error signal introduced by nonuniform electrical and mechanical properties of the area of the orbiting scroll baseplate observed by each probe. In order to accurately measure the electronic runout of each proximity probe, the drive train and orbiting scroll were assembled into the center portion of the semi-hermetic test shell as shown in Figure 5.

A computer program was written to acquire the proximity probe data at 10 degree intervals of crank angle while the shaft was rotated. The computer program fit a cubic spline through the runout data so that it could be digitally subtracted from the raw proximity probe signals acquired throughout the subsequent tests described below. It was possible to perform the digital signal processing on a real-time basis using the laboratory data system. Figure 6 shows one cycle of raw proximity probe data generated during operation of the laboratory compressor plotted with the electronic runout for probe 1. This figure clearly shows that a substantial portion of the raw signal can, indeed, be attributed purely to electronic runout rather than actual axial displacement of the orbiting scroll.

Compressor Startup

Figure 7 shows the suction, compression, and discharge pressures in the scroll compressor for approximately the first 60 shaft revolutions. These results showed that the laboratory scroll compressor approached full speed after only 3 to 4 shaft revolutions. The radial compliance mechanism engages quickly, resulting in compression pocket pressures which quickly approached their steady state values. As a consequence, the axial pressure force and overturning moment exerted on the orbiting scroll also quickly approached their steady state value. This required an axial compliance device which energized quickly to ensure negligible orbiting scroll wobble at startup. In order to optimize the axial compliance pressure chamber for transient startup conditions, a computer model similar to the steady state model described in Ref. [4] was developed for transient conditions.

The transient model used the transient pressures (Fig. 7) as input and assumed Fanno Flow (constant area, adiabatic, with friction) in the compliance chamber supply line. The conservation of mass, conservation of energy, and the refrigerant gas equation of state were used to calculate transient pressure in the compliance chamber according to the following equations:

For a scroll compressor equipped with a compliance chamber beneath an axially compliant orbiting scroll, the primary design criterion is to provide enough upward force beneath the orbiting scroll to not only overcome the downward compression force, but to counteract the orbiting scroll overturning moment as well. An optimum design would accomplish these functions with a minimum of excess upward force so as to minimize friction between the scroll elements. Upward force is generated by bleeding high pressure compression and/or discharge gas through the orbiting scroll baseplate into the compliance chamber.[4,5] If insufficient force is generated by the compliant chamber, even for a portion of the cycle, the orbiting scroll can become unstable, resulting in axial vibrations, or "wobble".

Much work has been done to ensure stability of the orbiting scroll during steady state operation. In typical compressor applications, however, a scroll compressor will spend much of its lifetime cycling on and off. To ensure maximum reliability, it is therefore prudent to design an axial compliance device which is not only stable at steady state conditions, but results in minimal instability during transient compressor startup and shutdown conditions. Accordingly, an analytical dynamic model of the orbiting scroll, applicable to steady state and transient conditions, is under development for use as a design optimization tool for axial compliance mechanisms [6]. In order to validate this model, and to gain valuable insight into the behavior of a scroll compressor during the first several seconds immediately after startup and shutdown, a laboratory prototype compressor was extensively instrumented and tested during transient and steady state operation.

EXPERIMENTAL PROCEDURE

Instrumentation

To perform the experiments described in this paper, the laboratory test compressor was instrumented with 4 high response proximity probes and 7 high response pressure transducers. For a 3-D rigid body, the coordinates of any three points are sufficient to describe rigid body motion. Accordingly, three proximity probes, located approximately 120 degrees apart, were installed beneath the orbiting scroll to measure the axial displacement of the orbiting scroll baseplate. A fourth proximity probe was installed to generate a signal which featured a sharp pulse at a known crank angle for use as a crank angle reference and speed pickup. Figure 1 shows the installation locations of the proximity probes.

One high response pressure transducer was located in the axial compliance chamber beneath the orbiting scroll (Fig. 1) to measure instantaneous pressure within the chamber. The remaining six high response pressure transducers were located in the fixed scroll to measure instantaneous suction, compression, and discharge port pressures. These pressure transducers were used to track the pressure of a fluid element as it traveled from suction to discharge during steady state or transient compressor operation [7]. Figure 2 shows the installation locations of the pressure transducers.

Data System

The data were acquired, stored, reduced, displayed, and plotted using a state-of-the-art data system at United Technologies Research Center (UTRC). This completely software driven data system features a real-time data acquisition computer and X-window terminals at 5 separate calorimeter and desuperheater test stands. The system is configured with multiple thermocouple channels, steady state channels, and high speed channels, and is shown schematically in Figure 3.

DYNAMICS OF AN ORBITING SCROLL WITH AXIAL COMPLIANCE
Part 2 - Experimental Techniques

Anthony J. Marchese
(203)727-7785
Assistant Research Engineer

United Technologies Research Center
Silver Lane - M.S. 19
East Hartford, CT 06108

ABSTRACT

In scroll compressors equipped with axial compliance mechanisms, the orbiting scroll may be exhibit axial motion, particularly during transient conditions at startup and shutdown. An experimental effort was undertaken to measure the instantaneous pressures acting on, and the rigid body motion of, an axially compliant orbiting scroll. For a rigid body, the <x,y,z> coordinates of any three points are sufficient to describe rigid body motion. Accordingly, three proximity probes located approximately 120 degrees apart, were installed beneath the orbiting scroll to measure the axial position of three points on the underside of the orbiting scroll baseplate. The remaining x and y coordinates were available from geometry and instantaneous crank angle measurement. High response axial compliance pressure, high response compression chamber pressures, and proximity probe data were acquired for various operating conditions at steady state, startup and shutdown. Results indicated that the duration of orbiting scroll "vobble" at transient startup conditions was a function of compliant chamber volume, port diameter and seal configuration. A computer model was written to optimize the compliance chamber to essentially eliminate the duration of orbiting scroll vobble during compressor startup. During compressor shutdown, the orbiting scroll remained stable.

NOMENCLATURE

C_v	Constant volume specific heat of refrigerant, btu/lbm-R.
d_{sl}	Diameter of compliance chamber supply line, in.
e_{sl}	Roughness of compliance chamber supply line, in.
h_{sl}	Enthalpy of gas entering compliance chamber, btu/lbm.
l_{sl}	Length of compliance chamber supply line, in.
m	Instantaneous mass in compliance chamber, lbm.
$\dot{m}_{sl}$	Instantaneous flow rate into compliance chamber, lbm/s.
p	Instantaneous pressure in compliance chamber, psia.
p_c	Instantaneous pressure in compression chamber, psia.
T	Instantaneous temperature in compliance chamber, R.
T_c	Instantaneous temperature in compression chamber, R.
t	Time, s.
V_{bc}	Compliance chamber volume, in^3.
v	Velocity of gas entering compliance chamber, ft/s.
z	Axial displacement of orbiting scroll baseplate, in.
z_c	Total axial clearance between scroll elements, in.
ρ	Instantaneous density of gas in compliance chamber, lb/in_3.

INTRODUCTION

In order to obtain high efficiency in a scroll compressor, some means of minimizing tip leakage is necessary. One method of minimizing tip leakage is to incorporate seals into the tips of the scroll flanks [1]. A second approach is to pressurize a cavity located beneath an axially compliant orbiting scroll. This approach generates an upward force on the orbiting scroll greater than the downward force generated by gas compression [2]. A third approach entails pressurizing a cavity above an axially compliant fixed scroll creating a downward force on the fixed scroll which is in excess of the upward pressure forces created by gas compression [3].

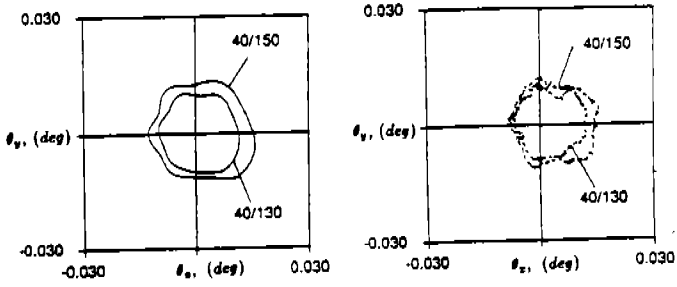

7a) analytical

7b) experimental

Fig. 7 Comparison of Wobble Results

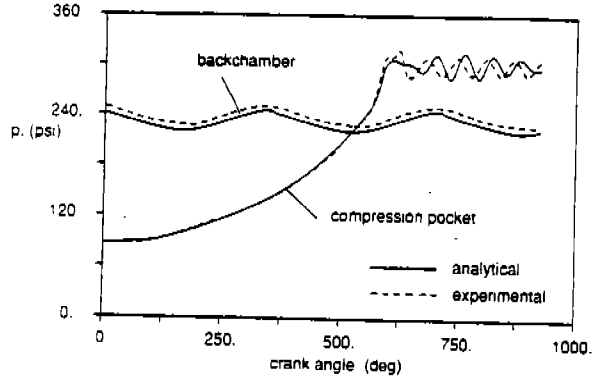

Fig. 4 Comparison of Analytical and Experimental Pressures

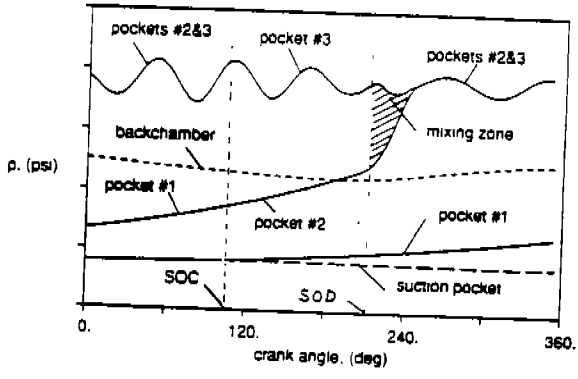

Fig. 5 Gas Pressures for Orbiting Scroll Dynamics Analysis

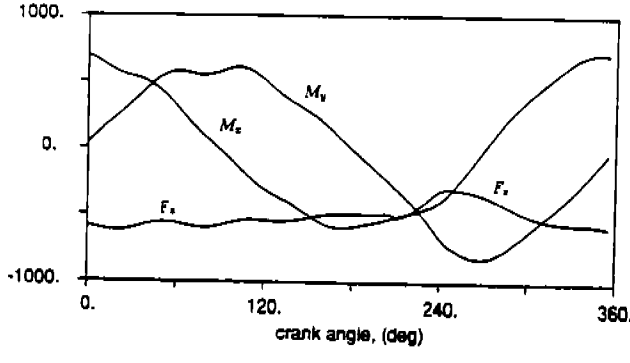

Fig. 6 Forcing Functions for Orbiting Scroll Dynamics Analysis

With these assumptions, both the axial component of the reaction force from fixed scroll and the force center required for preventing the orbiter from undergoing axial motion were computed. These data were converted into $F_x(t)$, $M_x(t)$ and $M_y(t)$ for the present study. However, in order to accept the experimental pressure data from any steady-state or transient operations, portions of the original simulation code were modified and integrated with the present model for use in predicting the transient dynamics for any given orbiting scroll design.

A set of the computed and measured pressures for the entire compression process for the same steady-state condition is shown in Fig. 4. Good agreement between the two are indicated. The pressures for all compression pockets and backchamber at any given crank angle, for one revolution, can be easily derived from these data, and results are shown in 5. These data are used for computing the three forcing functions and the results are shown in Fig. 6.

The effects of thermal and pressure loads on the axial growth of orbiting and fixed scroll wraps for various compressor operating conditions are under continuing study. Preliminary results of a finite element structural analysis indicated that the maximum axial growth always occurred at the inner tip of the scroll wrap and the predicted numerical value was approximately 0.0014 in for the test condition (Ref. 5). Based on this preliminary result and the design contours of the two scroll wrap heights, the axial contact constraint point (i.e. corresponding to λ_1 in Fig. 2) would occur near the inner tip of the scroll wrap and cause the orbiter to undergo small wobbles. The predicted orbiting scroll wobble characteristics based on this wrap tip constraint for two high pressure, high load, steady-state operating conditions are shown in Fig. 7a, and those obtained from the experimental study are shown in Fig. 7b. Good agreement between the two is indicated. Both the analytical and experimental results have indicated that the orbiter wobble motions are quite small, and the experimental results showed no impact on the operation of this experimental compressor.

5. CONCLUSIONS

Results of this study indicated that the wrap height contours of both the orbiting and fixed scrolls, which vary with compressor operating conditions, play an important role in the study of orbiter dynamics. The importance of constraints in the dynamic analysis of a given orbiter design is shown. The model presented is capable of predicting the orbiter dynamics of axial motion for steady-state or start-up operation if the wrap heights of both the fixed and orbiting scrolls, the thrust surface, bearing and seal clearences, and the pressure data surrounding the orbiting scroll are prescribed.

6. ACKNOWLEDGEMENT

The authors would like to thank Messrs. D.G. Cutts, R.L. DeBlois, A.J. Marchese, D.J. McFarlin and J.J. Nieter of UTRC and Mr. T. Kassouf of Carrier for their discussions, suggestions and comments during the course of this study.

REFERENCES

1. Marchese, A.J., "Dynamics of An Orbiting Scroll with Axial Compliance, Part - 2 Experimental Techniques", presented at the 1992 Int. Compressor Eng. Conf. at purdue, July 12-14, 1992.

2. Nieter, J.J. and T. Barito, "Dynamics of Compliance Mechanisms in Scroll Compressors, Part I: Axial Compliance" Proceeding of 1990 Int. Compressor Eng. Conf. at Purdue, Vol. 1, pp. 308-316.

3. Ishii, N. et al., "Dynamic Behavior of a Scroll Compressor", JSME International J. Series III, Vol.31, No. 1, 1988.

4. Morishita, E. et al., "Scroll Compressor Dynamics", Bulletin of JSME, Vol. 29, No. 248, Feb. 1986.

5. Marler, M.E. and K.B. Kumar, "Determination of Scroll Wrap Contact Stresses Using the Boundary Element Method", presented at the 1992 Int. Compressor Eng. Conf. at purdue, July 12-14, 1992.

The normalized equations of motion become

$$\begin{bmatrix} 1 & -\bar{e}_{cy} & \bar{e}_{cx} \\ -\bar{e}_{cy} & \bar{I}_{xx} & -\bar{I}_{xy} \\ \bar{e}_{cx} & -\bar{I}_{xy} & \bar{I}_{yy} \end{bmatrix} \begin{Bmatrix} \ddot{\bar{z}}_o \\ \ddot{\bar{\theta}}_x \\ \ddot{\bar{\theta}}_y \end{Bmatrix} + \begin{bmatrix} 2\sum_i \bar{c}_i \bar{r}_i & 0 & 0 \\ 0 & \sum_i \bar{c}_i \bar{r}_i^3 & 0 \\ 0 & 0 & \sum_i \bar{c}_i \bar{r}_i^3 \end{bmatrix} \begin{Bmatrix} \dot{\bar{z}}_o \\ \dot{\bar{\theta}}_x \\ \dot{\bar{\theta}}_y \end{Bmatrix} +$$

$$\begin{bmatrix} 2\sum_i \bar{k}_i \bar{r}_i & 0 & 0 \\ 0 & \sum_i \bar{k}_i \bar{r}_i^3 & 0 \\ 0 & 0 & \sum_i \bar{k}_i \bar{r}_i^3 \end{bmatrix} \begin{Bmatrix} \bar{z}_o \\ \bar{\theta}_x \\ \bar{\theta}_y \end{Bmatrix} = \begin{Bmatrix} \bar{F}_z - g_c \\ \bar{M}_x - g_c\, \bar{e}_{cy} + \bar{e}_{cz}\Omega^2 \bar{r}_o sin\ \Omega t \\ \bar{M}_y + g_c\, \bar{e}_{cx} + \bar{e}_{cz}\Omega^2 \bar{r}_o cos\ \Omega t \end{Bmatrix} \tag{20}$$

and the normalized constraint equations are

$$\begin{bmatrix} -1 & (\bar{r}_1)_{tip}\ sin\ \phi_c & -(\bar{r}_1)_{tip}\ cos\ \phi_c \\ 0 & (\bar{z}_2)_{tip}\ sin\ \phi_c & -(\bar{z}_2)_{tip}\ cos\ \phi_c \\ 0 & (\bar{z}_3)_{tip}\ sin\ \phi_c & (\bar{z}_3)_{tip}\ cos\ \phi_c \\ 0 & (\bar{z}_4)_{tip}\ sin\ \phi_c & -(\bar{z}_4)_{tip}\ cos\ \phi_c \\ 0 & (\bar{z}_5)_{tip}\ sin\ \phi_c & -(\bar{z}_5)_{tip}\ cos\ \phi_c \\ -1 & \bar{r}_{ts}\ sin\ \phi_c & -\bar{r}_{ts}\ cos\ \phi_c \\ 1 & \bar{r}_{cc}\ sin\ \phi_c & -\bar{r}_{cc}\ cos\ \phi_c \\ 0 & \bar{z}_{br}\ sin\ \phi_c & -\bar{z}_{br}\ cos\ \phi_c \end{bmatrix} \begin{Bmatrix} \bar{z}_o \\ \bar{\theta}_x \\ \bar{\theta}_y \end{Bmatrix} \leq \begin{Bmatrix} (\Delta\bar{r}_1)_{tip} \\ (\Delta\bar{r}_2)_{tip} \\ (\Delta\bar{r}_3)_{tip} \\ (\Delta\bar{r}_4)_{tip} \\ (\Delta\bar{r}_5)_{tip} \\ \Delta\bar{z}_{ts} \\ \Delta\bar{z}_{cc} \\ \Delta\bar{r}_{br} \end{Bmatrix} \tag{21}$$

Because 1) the equations of motion are coupled through the inertia term, 2) the constraint equations are nonlinear and must be checked at every integration step, and 3) the violated constraint equations must be solved simultaneously with the equations of motion, the numerical solution could exhibit stability problems. Therefore the Newmark method was chosen to solve the above dynamics equations because it provides stable numerical solutions to this type of problem.

4. CASE STUDY

The present study is based on design data for an experimental scroll compressor tested in the UTRC compressor laboratory described in a companion paper (Ref. 1).

4.1 Results of Undamped Free Vibration Analysis

The undamped free vibration analysis was performed to identify the system natural frequencies, and the first three harmonic values are 265.68 Hz, 201.04 Hz, and 192.02 Hz respectively. These results indicated that this compressor would not have any resonant problem during steady-state 60 Hz operation.

4.2 Results of Forced Response Analysis

As shown in Eq. (7), the equations of motions require three input forcing functions, $F_z(t)$, $M_x(t)$ and $M_y(t)$. These data were provided by a UTRC quasi-static simulation code. This simulation code is actually the first generation of the UTRC scroll compressor design code, which has been extensively used by Carrier to provide the basic design information for any given scroll compressor capacity and steady-state operating condition. Some of the assumptiuons used in the development of this simulation code are summarized below.

1. The orbiter undergoes a circular orbiting motion around the fixed scroll only in the (X, Y)-plane.
2. The gas pressures surrounding the orbiter are analytically determined at any crank angle for a given steady-state operating condition.
3. The body force and all external loads (including contact forces between the scroll flanks, between the orbiter baseplate and Oldham coupling ring, between the hub bearing and slider block) are in equilibrium with the linear inertia forces in the axial, radial and tangential directions.
4. Summations of all moments in the axial, radial and tangential directions for each hardware component are zero.
5. The inertia effects are considered in every time step, but not carried over to the following step (i.e. quasi-static assumption).

$$If\ z_{f1} \geq z_{o1}\ and\ z_{f1} \geq h_{tip},\ then \begin{cases} (\Delta z_1)_{tip} = 0 \\ \Delta z_{ts} = (z_{f1})_{tip} \quad h_{tip} \\ \Delta z_{cc} = z_{ac} - \Delta z_{ts} - z_{bp} \end{cases}$$

Equation (16) defines which of the axial clearance constraints are activated. It should be noted that the wrap tip and thrust surface constraints can be activated simultaneously or one at a time.

2.4 Equations of Motion with Constraints

It is obvious that if any conditional holonomic constraints are violated, there will be reaction forces exerted on the orbiter at the contact points as shown in Fig. 2. These contact forces can be represented by Lagrange multiplier λ_i. The equations of motion with two constraints, as an example, are given below.

$$\begin{bmatrix} m & -e_{cy}m & e_{cx}m & 0 & 0 \\ -e_{cy}m & I_{xx} & -I_{xy} & 0 & 0 \\ e_{cx}m & -I_{xy} & I_{yy} & 0 & 0 \\ 0 & 0 & 0 & 0 & 0 \\ 0 & 0 & 0 & 0 & 0 \end{bmatrix} \begin{Bmatrix} \ddot{z}_o \\ \ddot{\theta}_x \\ \ddot{\theta}_y \\ 0 \\ 0 \end{Bmatrix} + \begin{bmatrix} 2\pi \sum_i c_i r_i & 0 & 0 & 0 & 0 \\ 0 & \pi \sum_i c_i r_i^3 & 0 & 0 & 0 \\ 0 & 0 & \pi \sum_i c_i r_i^3 & 0 & 0 \\ 0 & 0 & 0 & 0 & 0 \\ 0 & 0 & 0 & 0 & 0 \end{bmatrix} \begin{Bmatrix} \dot{z}_o \\ \dot{\theta}_x \\ \dot{\theta}_y \\ 0 \\ 0 \end{Bmatrix} +$$

$$\begin{bmatrix} 2\pi \sum_i k_i r_i & 0 & 0 & -a_{i1} & -a_{j1} \\ 0 & \pi \sum_i k_i r_i^3 & 0 & -a_{i2} & -a_{j2} \\ 0 & 0 & \pi \sum_i k_i r_i^3 & -a_{i3} & -a_{j3} \\ a_{i1} & a_{i2} & a_{i3} & 0 & 0 \\ a_{j1} & a_{j2} & a_{j3} & 0 & 0 \end{bmatrix} \begin{Bmatrix} z_o \\ \theta_x \\ \theta_y \\ \lambda_i \\ \lambda_j \end{Bmatrix} = \begin{Bmatrix} F_z - mg_c \\ M_x \quad mg_c e_{cy} - e_{cx} m\Omega^2 r_o sin\Omega t \\ M_y + mg_c e_{cx} + e_{cx} m\Omega^2 r_o cos\Omega t \\ \Delta b_i \\ \Delta b_j \end{Bmatrix} \tag{17}$$

where $a_{i1}, a_{i2}, a_{i3}, a_{j1}, a_{j2}, a_{j3}, \Delta b_i$, and Δb_j are the coefficients and constant clearances of the violated i^{th} and j^{th} constraint equations.

3. METHOD OF SOLUTION

Because the coefficients of the equations of motion contain material and inertia properties of the orbiting scroll and backchamber seals, the numerical values of the matrix elements vary greatly in magnitude. To avoid any truncation errors in the numerical integration, all dependent and independent variables are normalized to have numerical values in the order of one. The referenced parameters chosen for this normalization process are

$$\begin{aligned} &z_n = \Delta t^2, \qquad \theta_n = \Delta t^2 / r_{bp}, \qquad I_n = m\, r_{bp}^2, \\ &c_n = m/(\pi\, r_{bp}\, \Delta t), \quad k_n = m/(\pi\, r_{bp}\, \Delta t^2) \end{aligned} \tag{18}$$

where Δt is the integration time step and r_{bp} is the radius of the baseplate. The normalized dependent and independent parameters for the equations of motion and constraints are listed below.

$$\begin{aligned} &\bar{z}_o = z_o/z_n, \qquad \bar{\theta}_x = \theta_x/\theta_n, \qquad \bar{\theta}_y = \theta_y/\theta_n, \\ &\dot{\bar{z}}_o = \dot{z}_o/\Delta t\ z_n, \qquad \dot{\bar{\theta}}_x = \dot{\theta}_x/(\Delta t\ \theta_n), \qquad \dot{\bar{\theta}}_y = \dot{\theta}_y/(\Delta t\ \theta_n), \\ &\ddot{\bar{z}}_o = \ddot{z}_o/(\Delta t^2\ z_n), \qquad \ddot{\bar{\theta}}_x = \ddot{\theta}_x/(\Delta t^2\ \theta_n), \qquad \ddot{\bar{\theta}}_y = \ddot{\theta}_y/(\Delta t^2\ \theta_n), \\ &\bar{r}_i = r_i/r_{bp}, \qquad \bar{c}_i = c_i/c_n, \qquad \bar{k}_i = k_i/k_n, \\ &\bar{I}_{xx} = I_{xx}/I_n, \qquad \bar{I}_{yy} = I_{yy}/I_n, \qquad \bar{I}_{xy} = I_{xy}/I_n, \\ &\bar{e}_{cx} = e_{cx}/r_{bp}, \qquad \bar{e}_{cy} = e_{cy}/r_{bp}, \qquad \bar{e}_{cz} = e_{cz}/r_{bp}, \qquad \bar{r}_o = r_o/r_{bp}, \\ &\bar{t} = t/\Delta t, \qquad \bar{r}_{ts} = r_{ts}/r_{bp}, \qquad \bar{r}_{br} = r_{br}/r_{bp}, \qquad \bar{e}_f = e_f/r_{bp}, \\ &\bar{r}_i = r_i/r_{bp}, \qquad \Delta\bar{z}_i = \Delta z_i/z_n, \qquad \Delta\bar{r}_i = \Delta r_i/z_n, \qquad \bar{F}_z = F_z/m \end{aligned} \tag{19}$$

By refering to Fig. 2, the constraint equations for the thrust surface, hub bearing, and crank case can also be derived as follows.

$$\begin{aligned} \rho_{ts}\, sin(\varphi_{ts} - \theta_w) - z_{bp} - z_o &\le \Delta z_{ts} \quad for\ \lambda_6 \\ z_o + r_{cc}\, sin\, \theta_w &\le \Delta z_{cc} \quad for\ \lambda_7 \\ r_{br} - \rho_{br}\, sin(\varphi_{br} - \theta_w) &\le \Delta r_{br} \quad for\ \lambda_8 \end{aligned} \tag{12}$$

where

$$\begin{aligned} \rho_{ts} &= \sqrt{z_{bp}^2 + r_{bp}^2}, \quad \varphi_{ts} = sin^{-1}(r_{bp}/\rho_{ts}) \\ \rho_{br} &= \sqrt{z_{hb}^2 + r_{br}^2}, \quad \varphi_{br} = sin^{-1}(r_{br}/\rho_{br}) \end{aligned} \tag{13}$$

It should be noted that the eight constraint equations shown in Eqs. (8) and (12) are nonlinear conditional holonomic constraints, and they must be checked at every integration step to see if they are violated. Once one or more constraints are violated, the motion of the orbiter is defined in part by the constraint condition, in which case the equal sign in the appropriate constraint equation defines the relationship that must geometrically exist during the time that the constraint condition is in place. During those time intervals, the constraint equations must be solved with the equations of motion, as described below. It is also important to note that θ_x, θ_y, and θ_w are always small (i.e. less than 0.1 degrees, or 0.002 radians), and Eq. (11) can be approximated by the following relation.

$$\theta_w \simeq (sin\ \phi_c)\, \theta_x - (cos\ \phi_c)\, \theta_y \tag{14}$$

After some mathematical manipulations, the eight constraint equations can be simplified to the following form.

$$\begin{bmatrix} -1 & (r_1)_{tip}\, sin\ \phi_c & -(r_1)_{tip}\, cos\ \phi_c \\ 0 & (z_2)_{tip}\, sin\ \phi_c & -(z_2)_{tip}\, cos\ \phi_c \\ 0 & (z_3)_{tip}\, sin\ \phi_c & -(z_3)_{tip}\, cos\ \phi_c \\ 0 & (z_4)_{tip}\, sin\ \phi_c & -(z_4)_{tip}\, cos\ \phi_c \\ 0 & (z_5)_{tip}\, sin\ \phi_c & -(z_5)_{tip}\, cos\ \phi_c \\ -1 & r_{ts}\, sin\ \phi_c & -r_{ts}\, cos\ \phi_c \\ 1 & r_{cc}\, sin\ \phi_c & -r_{cc}\, cos\ \phi_c \\ 0 & z_{br}\, sin\ \phi_c & -z_{br}\, cos\ \phi_c \end{bmatrix} \begin{Bmatrix} z_o \\ \theta_x \\ \theta_y \end{Bmatrix} \le \begin{Bmatrix} (\Delta z_1)_{tip} \\ (\Delta r_2)_{tip} \\ (\Delta r_3)_{tip} \\ (\Delta r_4)_{tip} \\ (\Delta r_5)_{tip} \\ \Delta z_{ts} \\ \Delta z_{cc} \\ \Delta r_{br} \end{Bmatrix}, \quad or \tag{15}$$

$$a_{jk} q_k \le \Delta b_j, \quad j = 1, ..., 8,\ k = 1, 2, 3$$

2.3 Clearances of Motion Constraints

The instantaneous clearances of the orbiter motion constraints for the right-hand side of Eqs. (15) must be specified. The instantaneous wrap tip clearances, $(\Delta r_2)_{tip}, ..., (\Delta r_5)_{tip}$ can be computed from the geometric locations of the scroll profiles. The hub bearing clearance, Δr_{br}, can be obtained from the design geometry. However, because the heights of the scroll wraps are usually contoured to accommodate the expected thermal expansions, the three axial clearances, $(\Delta z_1)_{tip}$, Δz_{ts}, and Δz_{cc} are related to the wrap heights of the fixed and orbiting scrolls at the contact points and the static axial clearance between the fixed scroll and the crank case, Δz_{ac} as shown in Fig. 2. If finite element structural analysis results are available, the wrap deflection data can also be incorporated into this analysis. Assuming the heights of the fixed and orbiting scroll wraps at the axial contact point are z_{f1} and z_{o1}, the height of the fixed scroll wrap at the thrust surface is h_{tip}, then we have the following relationships.

$$If\ h_{tip} \ge z_{f1}\ and\ h_{tip} \ge z_{o1},\ then \begin{cases} (\Delta z_1)_{tip} = h_{ttp} \quad MAX[(z_{o1})_{tip}, (z_{f1})_{tip}] \\ \Delta z_{ts} = 0 \\ \Delta z_{cc} = z_{ac} - \Delta z_{ts} - z_{bp} \end{cases}$$

$$If\ z_{o1} \ge z_{f1}\ and\ z_{o1} \ge h_{tip},\ then \begin{cases} (\Delta z_1)_{tip} = 0 \\ \Delta z_{ts} = (z_{o1})_{tip} - h_{tip} \\ \Delta z_{cc} = z_{ac} - \Delta z_{ts} - z_{bp} \end{cases} \tag{16}$$

2.2 Equations of Motion Constraints

Figure 3 shows the details of five possible constraint points at the orbiting scroll wrap tips for any given θ_x and θ_y, where the dotted lines represent the wrap profiles of the fixed scroll, the solid lines represent those of the orbiting scroll, point #1 is possible axial contact point, and points #2 to 5 are the possible radial contact points. The geometric locations of these contact points at any given instant (or crank angle) are analytically defined. In other words, the gap between the two scroll wraps for any given θ_x, θ_y are analytically determined. Neglecting the film effects due to orbiter relative motions, the following constraint equations can be easily derived. Fig. 3 illustrates these contact points. Note that the scroll is oriented so that the rotation of the orbiter is along the line A-A.

$$
\begin{aligned}
(\rho_1)_{tip}\cos(\varphi_1 - \theta_w) - (z_1)_{tip} - z_0 &\le (\Delta z_1)_{tip} \quad for\ \lambda_1 \\
(r_2)_{tip} - (\rho_2)_{tip}\sin(\varphi_2 - \theta_w) &\le (\Delta r_2)_{tip} \quad for\ \lambda_2 \\
(r_3)_{tip} - (\rho_3)_{tip}\sin(\varphi_3 - \theta_w) &< (\Delta r_3)_{tip} \quad for\ \lambda_3 \\
(\rho_4)_{tip}\sin(\varphi_4 + \theta_w) - (r_4)_{tip} &\le (\Delta r_4)_{tip} \quad for\ \lambda_4 \\
(\rho_5)_{tip}\sin(\varphi_5 + \theta_w) - (r_5)_{tip} &\le (\Delta r_5)_{tip} \quad for\ \lambda_5
\end{aligned}
\tag{8}
$$

where

$$
\left.
\begin{array}{l}
(r_i)_{tip} = \sqrt{(x_i^2 + y_i^2)_{tip}} \\
(\rho_i)_{tip} = \sqrt{(x_i^2 + y_i^2 + z_i^2)_{tip}} \\
\varphi_i = \sin^{-1}((r_i)_{tip}/(\rho_i)_{tip})
\end{array}
\right\}, \quad i = 1, \ldots, 5 \tag{9}
$$

$$
\theta_w = \sin^{-1}(-\cos\phi_c \sin\theta_y + \sin\phi_c \sin\theta_x)\,. \tag{10}
$$

$$
\phi_c = \tan^{-1}(-\theta_x/\theta_y) \tag{11}
$$

and $(\Delta z_1)_{tip}$ represents the axial clearance between the tip of the orbiting scroll and the root of the fixed scroll at point #1, and $(\Delta r_2)_{tip}$,..., $(\Delta r_5)_{tip}$ are the radial gaps (or clearances) between points 2 and 2',..., 5 and 5' respectively.

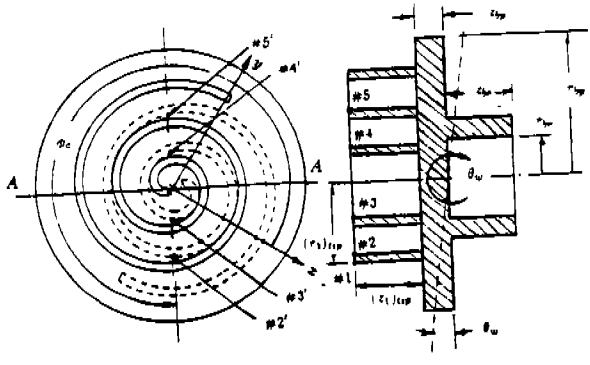

Fig. 3 Configuration of Constraint Models

$$= (F_z - mg_c - 2\pi \sum_i c_i r_i \dot{z}_o)\delta\dot{z}_o + (M_x - mg_c e_{cy} - \pi \sum_i c_i r_i^3 \dot{\theta}_x)\delta\theta_x + (M_y + mg_c e_{cx} - \pi \sum_i c_i r_i^3 \dot{\theta}_y)\delta\theta_y$$

By comparing the coeffieients of the virtual displacements of the three generalized coordinates, we have

$$Q_i = \{Q\} = \begin{Bmatrix} F_z - mg_c - 2\pi \sum_i c_i r_i \dot{z}_o \\ M_x - mg_c e_{cy} - \pi \sum_i c_i r_i^3 \dot{\theta}_x \\ M_y + mg_c e_{cx} - \pi \sum_i c_i r_i^3 \dot{\theta}_y \end{Bmatrix} \tag{5}$$

Finally, the equations of motion can be derived from the following Lagrange's equation.

$$\frac{d}{dt}\left(\frac{\partial L}{\partial \dot{q}_i}\right) - \frac{\partial L}{\partial q_i} = Q_i \tag{6}$$

where $L = T - V$ and q_i and $\dot{q}_i$ are the generalized coordinates $(z_o, \theta_x, \theta_y)$ and their time derivatives. By carrying out the differentiations of the Lagrange's equation and with the help of Eqs. (3), (4) and (5), we have three equations of motion for the orbiter axial motion, expressed in a matrix form as follows.

$$\begin{bmatrix} m & -e_{cy}m & e_{cx}m \\ -e_{cy}m & I_{xx} & -I_{xy} \\ e_{cx}m & -I_{xy} & I_{yy} \end{bmatrix} \begin{Bmatrix} \ddot{z}_o \\ \ddot{\theta}_x \\ \ddot{\theta}_y \end{Bmatrix} +$$

$$\begin{bmatrix} 2\pi \sum_i c_i r_i & 0 & 0 \\ 0 & \pi \sum_i c_i r_i^3 & 0 \\ 0 & 0 & \pi \sum_i c_i r_i^3 \end{bmatrix} \begin{Bmatrix} \dot{z}_o \\ \dot{\theta}_x \\ \dot{\theta}_y \end{Bmatrix} + \tag{7}$$

$$\begin{bmatrix} 2\pi \sum_i k_i r_i & 0 & 0 \\ 0 & \pi \sum_i k_i r_i^3 & 0 \\ 0 & 0 & \pi \sum_i k_i r_i^3 \end{bmatrix} \begin{Bmatrix} z_o \\ \theta_x \\ \theta_y \end{Bmatrix} = \begin{Bmatrix} F_z \quad mg_c \\ M_x - mg_c e_{cy} - e_{cz} m\Omega^2 r_o sin\Omega t \\ M_y + mg_c e_{cx} + e_{cz} m\Omega^2 r_o cos\Omega t \end{Bmatrix}$$

The orbiting scroll system natural frequencies and mode shapes can be computed using Eq. (7) by dropping both the damping and external load terms. However, because the orbiter is placed in a confined compartment, the forced response dynamics analysis must account for all possible constraints on the orbiter axial motion due to the fixed scroll, Oldham coupling ring, slider block, and crank case. Eight possible motion constraints are depicted in Fig. 2, and are indicated by the $\lambda_i, i = 1, 2, ...8$. It should be noted that λ_1 can occur at the wrap tip of either the orbiting or fixed scroll as shown in Fig. 2 and to be described further in Section 2.3.

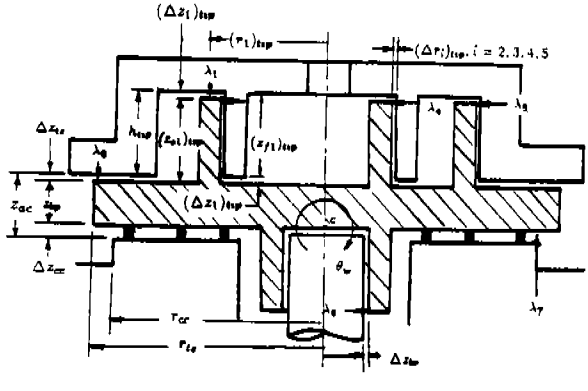

Fig. 2 Constraints of Orbiter Axial Motion

expressed in terms of these parameters as follows.

$$\vec{u}_p = [-(r_o sin\ \Omega t)\Omega dt + z\theta_y]\ \vec{i} + [(r_o cos\ \Omega t)\Omega dt - z\theta_x]\ \vec{j} + [y\ \theta_x - x\ \theta_y + z_o]\ \vec{k} \quad (1)$$

$$\dot{\vec{u}}_p = [-\Omega r_o sin\ \Omega t + z\dot{\theta}_y]\ \vec{i} + [\Omega r_o cos\ \Omega t - z\dot{\theta}_x]\ j + [y\ \dot{\theta}_x \quad x\ \dot{\theta}_y + \dot{z}_o]\ \vec{k} \quad (2)$$

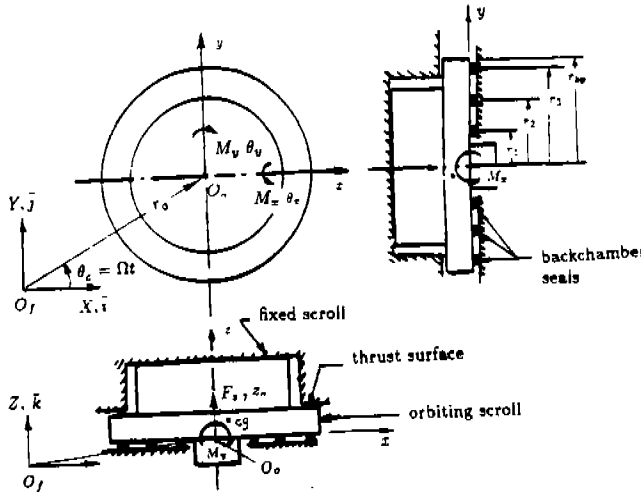

Fig. 1 Schematic Diagram of Orbiting Scroll Dynamics Model

The system kinetic energy (T) and potential energy (V) can be approximated by the following two equations.

$$\begin{aligned} T &= \frac{1}{2}\int_V \dot{\vec{u}}_p \cdot \dot{\vec{u}}_p\ dm \\ &= \frac{1}{2}r_o^2\Omega^2 m + \frac{1}{2}m\dot{z}_o^2 + \frac{1}{2}I_{xx}\dot{\theta}_x^2 + \frac{1}{2}I_{yy}\theta_y^2 - I_{xy}\dot{\theta}_x\dot{\theta}_y + e_{cy}m\dot{z}_o\dot{\theta}_x - e_{cx}m\dot{z}_o\dot{\theta}_y \\ &\quad -(e_{cx}m\Omega r_o cos\ \Omega t)\dot{\theta}_x - (e_{cx}m\Omega r_o sin\ \Omega t)\dot{\theta}_y \end{aligned} \quad (3)$$

$$\begin{aligned} V &= \sum_i V_i \equiv \sum_i \frac{1}{2}\int_0^{2\pi}[(\vec{u}_p \cdot \vec{k})^2]_i\ k_i\ r_i\ d\phi \\ &= \sum_i [\pi k_i r_i z_o^2 + \frac{\pi}{2}k_i r_i^3(\theta_x^2 + \theta_y^2)] \end{aligned} \quad (4)$$

where $m, e_{cx}, e_{cy}, I_{xx}, I_{yy}, I_{xy}$ are the orbiter mass, center of gravity, and moments and products of inertia, and $k_i, i = 1,2,3$, are the backchamber seal stiffnesses per unit length.

The system generalized forces Q_i can be derived in terms of the axial load, F_z, moments, M_x and M_y, body force, mg_c, and seal damping values, $c_i, i = 1,2,3$, using the following virtual work concept.

$$\begin{aligned} \delta W &= Q_1\ \delta z_o + Q_2\ \delta\theta_x + Q_3\ \delta\theta_y \\ &= (F_z - mg_c)\delta z_o + (M_x - mg_c e_{cy})\ \delta\theta_x + (M_y + mg_c e_{cx})\ \delta\theta_y - \\ &\quad \int_0^{2\pi}(\textstyle\sum_i c_i r_i d\phi)(\dot{u}_p \delta u_p)_{z=0} \end{aligned}$$

DYNAMICS OF AN ORBITING SCROLL WITH AXIAL COMPLIANCE
PART 1 - SIMULATION OF ORBITER AXIAL MOTION

H.T. Shu and A.A. Peracchio
United Technologies Research Center
Silver Lane · M.S. 19
East Hartford, CT 06108

ABSTRACT

A dynamic model was developed for investigating the axial motion of an orbiting scroll design which incorporates passive axial and radial compliance mechanisms. The model uses three degrees of freedom to describe the orbiting scroll axial motion. It also includes contact constraints for the thrust surface, the wrap tip and flanks, the crank case, and the hub bearing. The equations of motion were derived using the Lagrangian formulation. The system natural frequencies were predicted, and forced response analyses were performed. Results of the orbiting scroll dynamics analysis not only show good agreement with the experimental data, but also highlight the importance of the constraints.

1. INTRODUCTION

A comprehensive research program has been undertaken by the United Technologies Research Center (UTRC) to develop improved understanding of scroll compressor performance and dynamics in support of Carrier's product applications. This research program consists of not only extensive analytical modeling but also experimental investigation of system performance, pressures, temperatures, vibrations, and dynamic characteristics using instrumented compressors (Ref. 1). In this paper, a simulation of the orbiting scroll axial motion is presented.

Several investigations of scroll compressor dynamic behavior involving orbiter motion have been reported (Refs. 2 to 4). These studies (which usually include an orbiter, an Oldham coupling ring, an axial and radial compliance mechanism, and a crank shaft) have been developed using D'Alembert's principle to model the orbiter inertial effects. These studies assumed that the orbiter motion was constrainted to be in a plane perpendicular to the shaft centerline and within that plane, to execute a circular orbiting motion. Some have allowed for variations in shaft speed (Ref.3). The effect of damping and stiffness of the backchamber seal mechanism on the axial motion were not considered These studies have served as first generation scroll compressor design tools. However, in order to further improve understanding of compression efficiency, component reliability and compressor noise, the development of a more sophisticated dynamic model is required to account for additional degrees of freedom of motion and backchamber seal effects.

2. DYNAMIC MODELING

The dynamic model developed for investigating the scroll orbiter axial motion is described in this section. The model consists of three degrees of freedom represented by three generalized coordinates. It also accounts for motion constraints that might occur due to wrap tip contact with the mating baseplate, wrap flank contact with that of the fixed scroll at other than the ideal contact line, the thrust surface contact, motion constrained by the mechanical limits of the compression of the backchamber seals, and finally, contact of the orbiter hub with the drive shaft mechanism.

2.1 Equations of Motion

The schematic diagram of an orbiting scroll model is shown in Fig. 1, where F_z, M_x, and M_y represent the axial component of the time varying load and the x and y components of the time varying moments acting on the orbiter during comperssor operations. (Further descriptions of these three parameters will be given in the Case-Study Section.) The orbiter is supported by two or three backchamber seals with radii r_1, r_2, and r_3 respectively.

Let 1) (X_f, Y_f, Z_f) be the inertial coordinate system with origin O_f fixed at the shaft center, 2) (x, y, z) be the moving coordinate system with origin O_o fixed at the center of the baseplate bottom surface of orbiting scroll and always parallel to the inertial coordinate system throughout the entire compressor operation, 3) (r_o, Ω) be the radius of orbiting circle and shaft speed, and 4) $(z_o, \theta_x, \theta_z)$ be the generalized coordinates describing the orbiter axial translation and rotations of x and y axes. If z_o, θ_x, and θ_y are small, the displacement and velocity vectors of a small element of the orbiter at point $P(x, y, z)$ can be

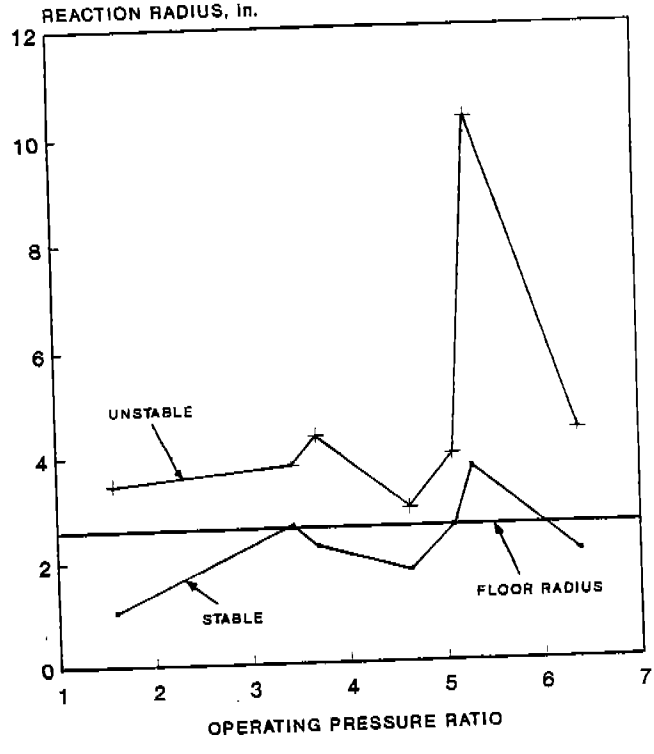
REACTION RADIUS, in.
12
10
8
6
4
2
0
1
2
3
4
5
6
7
UNSTABLE
STABLE
FLOOR RADIUS
OPERATING PRESSURE RATIO

Figure 5

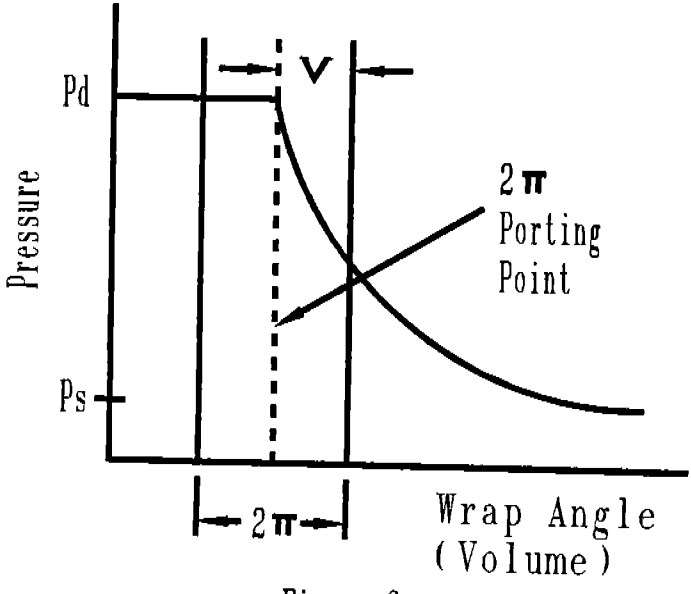

Figure 3

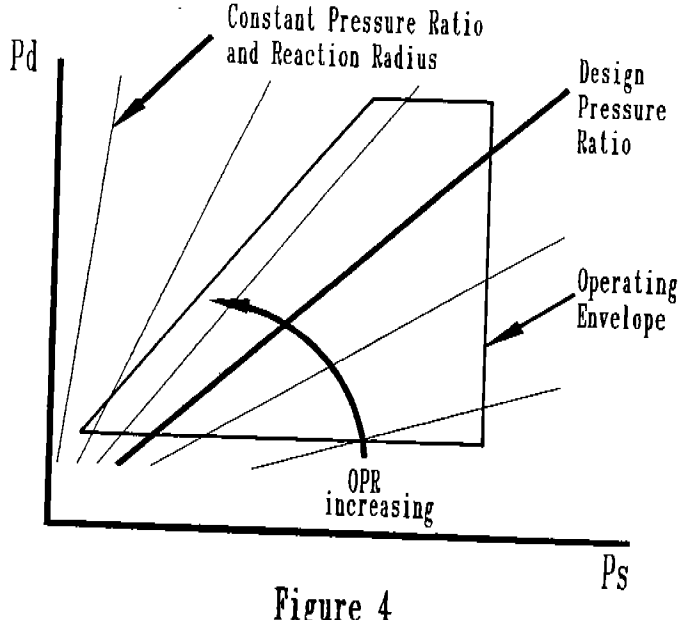

Figure 4

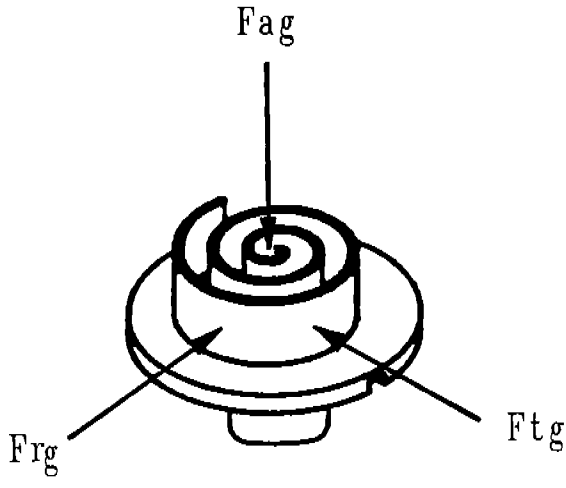

Figure 1

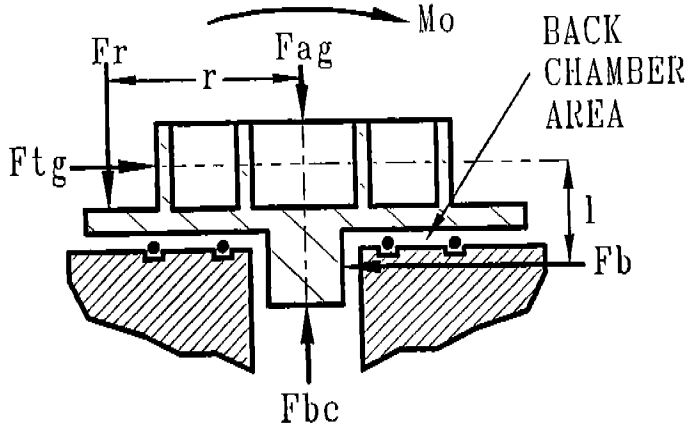

Figure 2

apply a correction factor based on experience with the particular compressor with which they work.

EXPERIMENTAL VERIFICATION

Figure 5 contains results of an experiment investigating the stability of a compressor with a back chamber supported orbiting scroll over a range of operating conditions and back chamber pressures. Scroll motion was monitored with internal proximity probes and the back chamber pressure was manually regulated from an external pressure source. For each condition, the pressure was slowly reduced until a rise in scroll wobble occurred. The reaction radius was calculated for the last pressure reading before instability and for the first reading after instability. These two radii are plotted with respect to operating pressure ratio. The marginally stable points are found to lie close to the line representing the physical radius of the scroll floor r. The lack of pressure feedback to the back chamber generally allowed for clear distinction between stable and unstable conditions, though in some cases, the transition from stable to unstable operation did not always occur instantaneously. This hints that the scroll may still have some limited self-stabilizing capability or simply that it is slow to respond to extremely brief excursions into an unstable operating zone.

CONCLUSION

The relationship derived above is a useful tool for designing stability into the axially compliant back-pressure supported orbiting scroll. It may be applied with equal effectiveness to either the single or dual chamber designs.

When peak reaction radii, calculated using peak loads, are greater than the radius of the floor for a portion of a revolution, static equilibrium does not exist and the orbiting scroll starts to experience a wobble or vibration that can quickly lead to loss of performance and premature failure of the compressor. However, positive pressure feedback from the sealed pockets to the back pressure chamber will cause the scroll to remain stable at conditions somewhat beyond those that these first order relationships predict.

REFERENCES

Some relevant publications in the study of axial compliance include:

1. COMPUTER MODELING OF SCROLL COMPRESSOR WITH SELF ADJUSTING BACK-PRESSURE MECHANISM; Tojo, Ikegawa, Maeda, Machida, Shiibayashi & Uchikawa; Hitachi Ltd; Japan. (1986 Purdue, p. 872).

2. PERFORMANCE ANALYSIS OF SCROLL COMPRESSOR FOR AIR CONDITIONERS; Hayano, Nagatomo, Sakata & Hatori; Toshiba Corp; Japan. (1986 Purdue, p.856).

3. A SCROLL COMPRESSOR FOR AIR CONDITIONERS; Tojo, Ikegawa, Shiibayashi, N.Arai, A.Arai & Uchikawa; Hitachi Ltd; Japan. (1984 Purdue, p.496).

4. DYNAMICS OF COMPLIANCE MECHANISMS IN SCROLL COMPRESSORS, PART I: AXIAL COMPLIANCE; Nieter & Barito; United Technologies Carrier, USA. (1990 Purdue, p. 308).

5. SCROLL COMPRESSOR DESIGN CRITERIA FOR RESIDENTIAL AIR CONDITIONING AND HEAT PUMP APPLICATIONS, PART I AND II; Bush & Elson; Copeland Corp. U.S.A. (1988 Purdue, p. 93).

STABILITY EQUATIONS

Rearranging the force and moment summation equations above to solve for r gives

$$r = \frac{F_{tg} l}{(F_{bc} - F_{ag})} \tag{1}$$

Substituting the force equations for Ftg, Fag, and Fbc gives:

$$r = \frac{l(C_1 P_s + C_2 P_d)}{A_{bc}\left[\frac{v}{2\pi}(C_0 - 1) P_s + \frac{2\pi - v}{2\pi}(P_d - P_s)\right] - C_3 P_s - C_4 P_d} \tag{2}$$

Simplifying and grouping terms for Ps and Pd results in:

$$r = \frac{[lC_1] P_s + [lC_2] P_d}{\left[A_{bc}\left(\frac{v}{2\pi} C_0 - 1\right) - C_3\right] P_s + \left[A_{bc}\frac{2\pi - v}{2\pi} - C_4\right] P_d} \tag{3}$$

Letting K1, K2, K3, and K4 represent the above bracketed terms, respectively, and dividing the numerator and denominator both by Ps, we have:

$$r = \frac{K_1 + K_2 OPR}{K_3 + K_4 OPR} \tag{4}$$

where OPR is the operating pressure ratio of the compressor. The reaction radius r is found to be constant for a given operating pressure ratio of the compressor.

A similar derivation and simplification for the "tip" or reaction force Fr gives:

$$F_r = P_s (K_3 + K_4 OPR) \tag{5}$$

DESIGN PROCEDURE

Lines of constant reaction radius are superimposed on an operating envelope in Figure 4. They correspond to constant operating pressure ratio lines. The design procedure is to choose two extreme design points in the operating envelope, for example the maximum and minimum expected operating pressure ratio points, and fix r equal to the radius of the orbiting scroll floor portion. This results in two linear equations which are solved simultaneously for the two unknowns of Abc and v. As a result, all other r values within the operating envelope will be less than the radius of the floor. This assures stability over the entire envelope. The final values of Abc and v must be chosen within the physical limits of the scroll compressor's layout.

In practice, use of peak loads will result in a very conservative design with higher tip loading than may be really required. When the compressor reaches an unstable operating condition, based on peak load calculation, it will begin to wobble for a small portion of the cycle while the peak loads exist. The resulting tip leakage causes higher pocket pressures which in turn feed back to the back chamber, raising its pressure as well. This positive feedback will hold the scroll in a quasi-stable condition beyond the expected stable operating range. On the other hand, use of average loads only will likely be insufficient to assure stability. Designers should

$$F_{tg}=C_1P_s+C_2P_d \quad (4)$$

$$F_{ag}=C_3P_s+C_4P_d \quad (5)$$

where Ps and Pd are the compressor suction and discharge pressures respectively. The constants C1 through C4 are functions of the particular scroll geometry. These force equations are derived to be "gage" forces, i.e, resulting from pressures above the "ambient" pressure Ps. The constants C1 through C4 may be derived to represent either average or peak forces. The timing of the peak force, whether axial or tangential, is dependent on whether the compressor is operating above or below the design pressure ratio. The peak force occurs just before the discharge porting point for operation below the design pressure ratio and just after porting for operation above the design pressure ratio. For this reason, the value of the four constant coefficients for peak loads will be different for the two zones of operation.

Back chamber pressure is typically provided by a combination of pressure from the discharge and from the sealed compression pockets. In this manner, the back chamber force may be made up of two components which behave in a similar manner, with respect to operating pressures, as do the internal gas forces. A common method is to provide two separate chambers for these force components. In that case, the back chamber force may be written as

$$F_{bc}=(C_0-1)\,P_sA_i+(P_d-P_s)\,A_d \quad (6)$$

where Co represents the time-average normalized pressure seen by a vent communicating between an intermediate pressure back chamber and a sealed compression pocket and Ai and Ad respectively are the areas of the intermediate and discharge back chambers. This method is most commonly applied in the high-side compliant orbiting scroll design and in the compliant fixed scroll design, in both of which it is convenient to provide discharge pressure at the center of the axially compliant scroll.

Another method especially suited to the low side compliant orbiting scroll design is to use a single back chamber whose vent is exposed to intermediate pressure for a portion of the time and to discharge pressure for the remainder. Figure 3 illustrates how such a vent hole sees the compression process. In this example Pd happens to be equal to the pressure in the sealed pockets as they open to discharge, but may vary independently. The vent is located at an angle v from the inner end of the wrap. In one revolution (or orbit) the vent sees the pressure in the sealed pocket for a period of $v/2\pi$, and it sees Pd for a period of $(2\pi-v)/2\pi$. The average pressure seen in the sealed pockets is calculated by assuming a polytropic compression process and solving an averaging integral which will result in the form Co Ps, where, similar to the two chamber design, Co is a function of the scroll geometry and now v. The back chamber pressure equation can be written as:

$$P_{bc}=\left(\frac{v}{2\pi}\right)(C_0-1)\,P_s+\left(1-\frac{v}{2\pi}\right)(P_d-P_s) \quad (7)$$

where Pbc is the average back chamber pressure. Note that this equation is of the same linear form as the back chamber force equation for the two chamber case. The back chamber force is found by simply multiplying the pressure by the chamber area:

$$F_{bc}=P_{bc}A_{bc} \quad (8)$$

compression chambers is admitted to sealed zones on the back of the orbiting scroll. The resulting force overcomes the axial separating force and pushes the orbiting scroll into contact with the fixed scroll. In addition to this, it is necessary to add an additional force increment to overcome a characteristic overturning moment which acts on the orbiting scroll.

In Figure 2 is a diagram of the forces acting on the orbiting scroll in the plane which is parallel to the axial and tangential gas forces. For this analysis, there is also an influence from the radial gas force, but it is very small and will be neglected for this first-order approximation. In addition to the gas forces, there is a force applied to the drive bearing of the orbiting scroll in response to the tangential gas force and a reaction force acting axially between the orbiting and fixed scrolls. Force summations in the axial and tangential directions are:

$$\Sigma F_a = 0 = F_{bc} - F_{ag} - F_r \qquad (1)$$

$$\Sigma F_t = 0 = F_{tg} - F_b \qquad (2)$$

where ΣFa is the axial force summation, Fbc is the net back chamber force, Fr is the scroll-to-scroll axial reaction force, and Fb is the scroll drive bearing force.

Since the tangential gas force and bearing reaction do not typically act on a single line, there is also an overturning moment associated with them:

$$\Sigma M = 0 = F_{tg} l - F_r r \qquad (3)$$

where l is the distance between the midpoint of the scroll vane and the drive bearing (the distance between Ftg and Fb). The value of the reaction radius, r, will vary according to the particular back-chamber design and operating condition.

ORBITING SCROLL STABILITY

If the theoretical value of the reaction radius should exceed the physical size of the orbiting or fixed scroll, whichever is smaller, it will in fact be confined to the physical edge of the part. Since a sufficient radius to balance the moment equation is unavailable, the moment summation will no longer be zero, the orbiting scroll will no longer be in static equilibrium, and it will start to overturn until it comes into contact with some other mechanical restraint. This action, coupled with the orbital movement of the scroll, results in a sort of wobbling motion with all the axial contact occurring along the edge of the part.

This wobbling, or instability, results in leakage through the gap opened by the separated tips, edge loading of the scroll surfaces, and angular misalignment of the scroll drive bearing. All these can quickly lead to loss of performance and premature failure of the compressor.

GAS FORCE EQUATIONS

The axial and tangential forces, whether expressed in peak or average terms, consist of two components. Part of each force is derived from the pressure in the sealed pockets, which is a function of scroll geometry and suction pressure only. The other part is derived from the pressure in the discharge pocket and is a function of scroll geometry and the suction to discharge pressure difference only. These forces can be written in the linear form:

GENERAL STABILITY AND DESIGN SPECIFICATION OF THE BACK-PRESSURE SUPPORTED AXIALLY COMPLIANT ORBITING SCROLL

James W. Bush
Program Manager

David K. Haller
Project Leader

Christopher R. Galante
Project Engineer

Scroll Compressor Design
United Technologies Carrier
Syracuse, New York 13221

ABSTRACT

A linear, first order relationship may be used to approximate the stability characteristic of the back-pressure supported orbiting scroll. The resulting average tip loads may be similarly represented. Operating zones of incipient orbiting scroll instability are found to approximately follow zones of constant compression ratio. A simple design procedure is presented which may be used to specify axial compliance parameters for stability over an arbitrary operating range and to estimate resulting tip loads.

INTRODUCTION

The scroll compressor commonly consists of one scroll orbiting with respect to a second, typically fixed, scroll. Hence the terms "orbiting scroll" and "fixed scroll". These scrolls each have a flat floor portion on which is an involute-shaped wrap. As the scrolls intermesh, a series of trapped pockets are formed which decrease in size as they travel towards the center, compressing the gas within. Ideally the tips and flanks of the wraps would always be in light contact for truly sealed pockets.

During compression, gas pressure acts against the scrolls to separate them both axially and radially. These forces must be countered by some mechanism or structure. In so-called compliant designs, the scrolls are brought into positive contact to properly seal pockets for efficient compression. The scrolls are held in place by external forces, usually gas-induced, which allow the scrolls to "float" and determine their own geometric relation to each other. This nonrigid support also allows the scrolls to separate in response to liquids or small debris which may be ingested.

Compliance in the radial direction is usually provided by mechanical means in the orbiting scroll drive. In this paper we focus on compliance in the axial direction and discuss the theory and design considerations for stable operation over an arbitrary range of conditions.

FORCES ON THE SCROLLS

The forces on the orbiting scroll resulting from the compression process are shown in Figure 1. The radial gas force, Frg, acts along the line between the centers of the two scrolls and tries to push them apart to a common center. The tangential gas force, Ftg, acts at the midpoint of and perpendicular to the line between the centers of the two scrolls. This is the force against which the actual work of compression is performed. The axial gas force, Fag, acts midway along the line between the two scrolls and normal to the plane of orbiting motion. This force tends to separate the scrolls axially. All forces act equally and symmetrically on both scrolls.

For axial compliance design, we must, as a beginning, overcome the influence of the axial gas force. For the back-pressure supported orbiting scroll, gas pressure from the sealed

CONCLUSION

(1) HFC 134a can be used instead of CFC 12 in the current refrigeration system. But the compressor design modification is needed for the sake of energy efficiency. Total of 20 % improvement of COP was achieved in this study.

(2) Lubricant
Hindered type ester shows better characteristics of lubricant than complex type ester. But a great amount of attention must be paid to the prevention of moisture penetration (less than 40 ppm) during compressor manufacture process as there still remains the possibility of hydrolysis.

(3) Material Compatibility
Both of polyester nylon and EI/AI wire can be used with HFC 134a/ester while it is necessary to review the compatibility of PET film in view of oligomer extraction.

ACKNOLEDGEMENT

The authors wish to thank Director Tadanori Kato of Japan sun oil co. and Manager Lee, jong man of Isu chemical co. for their contributions to this work through many experiments and discussions.

REFERENCES

(1) J. Kim and W. Soedel, " Performance and gas pulsations when pumping different gases with the same compressor.", 1988 Purdue compressor engineering conference.

(2) Hideki Kawai, " The development of high efficiency compressors by reducing suction gas temperature.", 1982 Purdue compressor engineering conference.

(3) John J. Jacobs, " Analytic and experimental techniques for evaluating compressor performance losses.", 1976 Purdue compressor engineering conference.

Table 5 Typical properties of lubricant

Lubricant	Type	viscosity (cst) 40 C	100 C	VI	T.A.N. (mgKOH/g)
Ester A	complex	31.5	5.8	133	0.01
Ester B	hindered	22.5	4.6	132	0.025
Ester C	hindered	31.49	5.22	102	0.01
Ester D	hindered	32.4	5.25	97	0.01

Test condition
Ps = 0.1 Mpa, Pd = 3.0 Mpa
Dome Temp. = 95 ~ 105 C
* metal content [ppm]

Table 6 Analysis of used Lub. (500 Hr life test)

Lub.	T.A.N. New	Used	Metal * Element Fe	Cu	Al
Ester A	0.01	0.26	10	1	1
Ester B	0.025	0.17	3	1	1
Ester C	0.01	0.01	5	1	1
Ester D	0.01	0.02	5	1	1
CFC 12 Mineral	0.01	0.30	5	1	1

Table 7 Hydrolysis

Lubricant	moisture (ppm)	T.A.N. (mgKOH/g)	Catalyst
Ester A	1000/170	0.025/3.6	Fe,Cu,Al
Ester B	1000/ 90	0.01/4.8	
Ester C	1000/150	0.01/3.1	
Ester D	1000/260	0.01/2.7	

Test condition
Lub / HFC 134a = 3 / 1 , Duration = 175 C , 14 days

Table 8 Effect of metal surface treatment

Metal element					
with s/t			without s/t		
Fe	Cu	Al	Fe	Cu	Al
5	1	1	10	1	1

MATERIAL COMPATIBILITY

The compatibility with HFC134a/ester mixture of all the construction material are tested by the autoclave test method or bomb test method and the results are compared with the one practiced with CFC 12/mineral oil mixture.

One thing to be appreciated is that it is difficult to draw a general conclusion as the compatibility test result is dependent on the characteristics of locally available materials and lubricant.

Compatibility of PET film

PET film currently being used with CFC 12 is not so compatible with HFC 134a/ester as CFC 12/mineral oil in view of oligomer extraction. But the one being used with HCFC 22 shows good compatibility with HFC 134a/ester. (Table 10)

Compatibility of magnetic wire

Both of polyester nylon and EI/AI wire shows compatibilty with HFC 134a/ester (Table 11).

Table 10 Compatibility of PET film

Material	Mixture	Oligomer wt %	Estimation
PET 1	R12/Mineral	0.28	Reference
PET 2	R12/Mineral	0.10	Better
PET 1	R134a/Ester C	0.53	Worse
PET 2	R134a/Ester B	0.05	Better
PET 2	R134a/Ester C	0.03	Better

Test condition 130 C x 40 Days
PET 1 for CFC 12 , PET 2 for HCFC 22

Table 11 Compatibility of magnetic wire

Material	Mixture	B D V [Kv] Before	After
Polyester	R12/Mineral	12	6
AI/EIW	R12/Mineral	12	11.6
Polyester	R134a/Ester C	12	11
AI/EIW	R134a/Ester C	12	10

Test condition 150 C x 7 Days
* No Blister was found.

this was also geometrically possible. 1.4 % increase of capacity and 2.3 % of COP were achieved by the modulation of residual volume.

Effect of low viscosity oil

Frictional loss can be reduced by the use of low viscosity oil. Fig. 4 shows the differences of power consumption between 32 cst and 15 cst lubricants. The effect of low viscosity oil is more remarkable when the shell temperature is low.

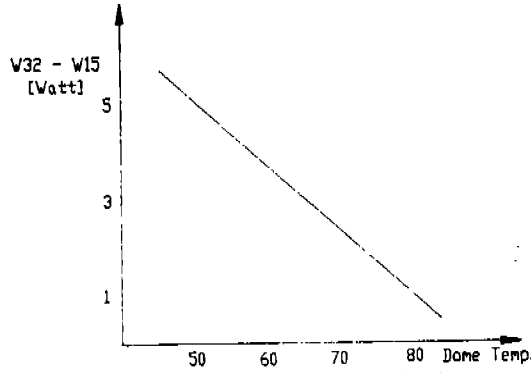

Fig. 4 Effect of low viscosity oil

Improvement of motor efficiency

While motor design of hermetic compressor is restricted by the required starting characteristics, reduction of the coefficient of friction by the surface treatment on the shaft and bearing makes room for the improvement of motor efficiency. Summing up all the effect of improved core material, reduced motor open slot, air gap, we could improve motor efficency from 70 % to 80 % . Table 4 shows the comparison of motor specifications.

Table 4
Motor improvement

core material	3 %
open slot	2 %
air gap	2 %
torque reduction	3 %

Fig.5 shows every effect of compressor design modifications.

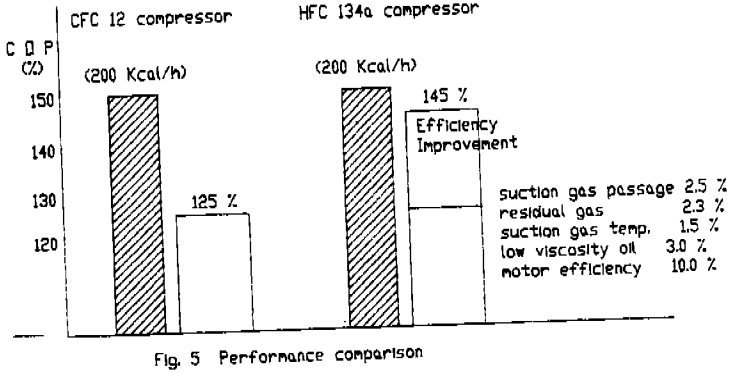

Fig. 5 Performance comparison

LUBRICANT

1 complex type ester and 3 hindered type esters are tested for the HFC 134a compressor (Table 5). The comparison was done by the T.A.N.(Total Acid Number) and metal contents in the life tested lubricants (Table 6). Although conventional method like falex load and wear test are very effective more emphasis was put on the real test.

The hydrolysis of esters may be regarded as one source of future troubles. Our simulative test is accelerating the hydrolysis by heat and intentionally added moisture. The hydrolysis is rated by the change of T.A.N. The test condition and result of lubricants' hydrolysis are described at Table 7. The effect of metal surface treatment on the wear is presented in Table 8. The influence of moisture on the wear is shown in Table 9.

Effect of suction gas temperature

There are many previous studies on the effect of suction gas temperature. Specific volume of suction gas is reduced as the decrease of suction gas temperature to increase the mass flow rate, while the gas compresson work is not so sensitive to the gas temperature./2/ It can be said that the effect of suction gas temperature is straight-forward and the amount of reduction simply depends on the system design. We could reduce 5 C of suction gas temperature to improve 2 % of capacity, 1.5 % of COP with the increased shell surface area (10 %) and nearer semi direct suction, shape improvement of suction inlet to prevent suction gas from being dispersed at the suction pipe.

Effect of suction pressure drop

As the pressure drop during suction process causes increase of specific volume and decrease of capacity, reduction of pressure drop results in improvement of capacity and efficiency. While suction loss can be divided into two parts — suction valve loss and suction passage loss, we simply confined our interest only to the suction passage loss, and reduction of pressure drop by 0.01 kgf/cm G showed 3 % increase of capacity, 2.5 % improvement of COP. The reduction of pressure drop was achieved by the simplification of suction muffler structure.(increase of A and decrease of L)

One thing to be mentioned here is that the cut-off frequency of suction muffler is shifted up due to the difference of sonic velocities in CFC 12 and HFC 134a. ($C_{134a} / C_{12} = 1.15$)

$$f_c = \frac{c}{2\pi}\sqrt{\frac{A}{L\,V}} \qquad (5)$$

As it can be said that compressor noise level is proportional to the cut-off frequency of suction muffler, this shift up may be regarded as one source of rather noisy HFC 134a compressor.

And also the shift up of cut-off frequency accompanied with the muffler structure must be reduced for the even compressor noise level. Table 3 summarizes these procesure.

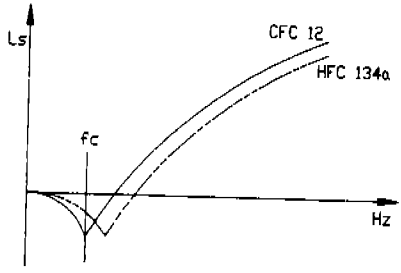

FIG. 2 SHIFT OF CUT-OFF FREQUENCY

Table 3. Shift up of suction muffler cut off frequency due to the difference of sonic velocity

	conventional design with CFC 12	conventional design with HFC 134a	proto-type design with HFC 134a	Improved design with HFC 134a
ratio of cut off frequency	1	1.15	1.8	1.1
noise level	reference	+ 1 - 2 dB	+ 3 dB	less than 1 dB
capacity	-	reference	+ 3 %	+ 3 %
C O P	-	reference	+ 2.5 %	+ 2.5 %

Effect of residual gas

Many previous studies on the effect of residual gas conclude that clearance volume can be optimised for any given piston and valve plate design. /3/

The residual gas prevent fresh new gas from being sucted during re-expansion process, while too small a clearance volume increases over-compression loss.

The performance was best at the 0.7 % clearance volume ratio, and

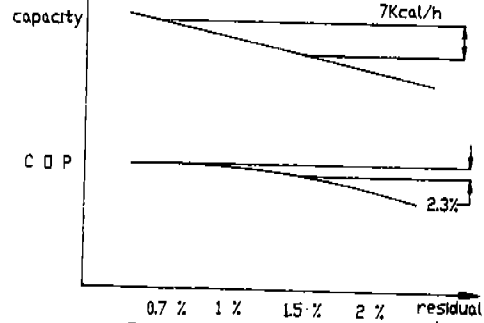

Fig. 3 Effect of residual gas

PERFORMANCE

(1) Model Compressor

Ball joint type reciprocating compressor is used for this study. This model is widely applicated in the domestic refrigeration market. Specification is summarized in Table 2.

Table 2
Specification

Capacity *	200 kcal/h
Bore	23.5 mm
Displacement	7.02 cc/rev
motor output	175 watt
Dimension	ϕ159 x H 170

* with CFC 12

(2) Method of approach

General losses in a reciprocating compressor are shown in Fig.1 for the purpose of brief overview. The mass flow rate, capacity, and COP may be written as equations (1),(2),(3).

$$\dot{m} = \frac{60\ N\ \eta_v\ V_d}{v_s} - \dot{m}_{leak} \qquad (1)$$

$$Q = \dot{m}\ \Delta h_{evs} \qquad (2)$$

$$COP = \frac{Q}{W} = \frac{\dot{m}\ \Delta h_{evs}}{W_{eff} + W_{loss}} \qquad (3)$$

Equation (3) is chosen as a objective function of this study. Each physical factors affecting the objective function will be reviewed. The way of approach is very simple, improvement of volumetric efficiency, reduction of specific volume to increase mass flow rate, and reduction of mechanical and electrical losses. Many previous studies were interested only in the reduction of energy losses to improve compressor efficiency, while this study is rather interested in the increase of mass flow rate as a tool of improving the COP. The degree of compressor design optimization will be measureded by the convergence of real mass flow rate to the ideal mass flow rate. For this purpose, one may define a new parameter coefficient of mass flow rate η_{mf} as follows.

$$\eta_{mf} = \frac{\text{real mass flow rate}}{\text{ideal mass flow rate}} \qquad (4)$$

Ideal mass flow rate is obtainable only when $\eta_v = 1$, $\dot{m}_{leak} = 0$, $\dot{m}_{lub} = 0$, suction gas preheat during suction process = 0. Therefore the way to the design modification is evident, $\eta_{mf} = 1$, $W_{loss} = 0$.

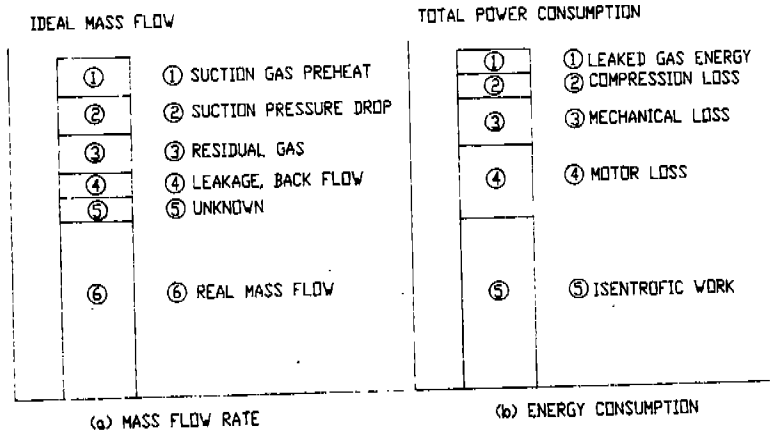

FIG. 1 GENERAL LOSSES IN A RECIPROCATING COMPRESSOR

AN EXPERIMENTAL INVESTIGATION OF A REFRIGERATION COMPRESSOR USING HFC 134a AS A WORKING SUBSTANCE

Cho Kwang Yeon, Shin Seung Hoon , Baik Woon Yong
Central Research & Development Laboratory, Daewoo Electronics,
Yong Hyon Dong, Incheon, Korea

Cho Cheol Yeon , Ho Jeong Hwan
Incheon Works, Daewoo Electronics, Ltd.
Yong Hyon Dong, Incheon, Korea

ABSTRACT

A proto type compressor using HFC 134a as a working substance is designed. As the specific volume of HFC 134a is larger than that of CFC 12,the mass flow rate and capacity are decreased. Reduction of residual gas and suction gas temperature and improvement of suction gas passage, motor efficiency, use of low viscocity oil are considered to improve the performance of a HFC 134a compressor. By these modifications, the COP of (Coefficient of Performance) HFC 134a compressor could be improved by 20 %. The results of compressor life tests and compatibility tests practiced with 4 kinds of ester oil are reported.

NOMENCLATURE

A	area of suction muffler inlet	V	suction muffler volume
c	speed of sound	Vd	displacement
fc	cut off frequency of suction muffler	v_s	specific volume
L	length of suction muffler inlet	W_{eff}	isentropic work
Ls	Attenuation	W_{loss}	energy loss during gas compression
$\dot{m}$	mass flow rate	W_{32}	energy consumption using 32 cst oil
$\dot{m}_{leak}$	leakage	W_{15}	energy consumption using 15 cst oil
Q	capacity	N	rpm
Δh_{evs}	difference of enthalpy between evaporator outlet and inlet	η_v	volumetric efficiency

INTRODUCTION

After the publication of the critical effect of the CFCs on the earth's atmosphere, extensive works have been done to search for new refrigerant to substitute for CFCs. CFC 12 has been widely used as a refrigerant in the refrigeration field due to its excellent thermodynamic properties, chemical stability, non-toxicity, non-flammability.

HFC 134a, although it does not possess all the necessary and sufficient conditions, is currently being studied to replace the CFC 12 as it has relatively similar thermodynamic properties with CFC 12.

The problems to be solved to use HFC 134a as a new refrigerant may be listed as follows.

(1) Performance
(2) Development of new lubricant
(3) Material compatibility

It can be said that one of difficult problems of HFC 134a is a capacity drop resulted from its relatively large specific volume. (Table 1) Although this capacity drop may be easily compensated for by the simple increase of displacement volume, it is more effective to find ways to increase mass flow rate with current displacement volume as it is not always possible to increase displacement volume and it does not imply improvement of efficiency.

Table 1.

	HFC 134a	CFC 12
$\dot{m}$	0.7	1
Δh_{evs}	1.24	1
Q	0.87	1

As HFC 134a shows very poor miscibility with mineral oil, it is necessary to develop new lubricant miscible with HFC 134a. Although much work has been done with PAG, polyol ester shows more possibility than PAG in view of hygroscopicity and lubricity. However thermal stability, hydrological stability, still need to be estimated for the compressor reliability. This study is to review measures to improve a compressor performance, to discuss lubricant problem and materials compatibility using HFC 134a as a working fluid.

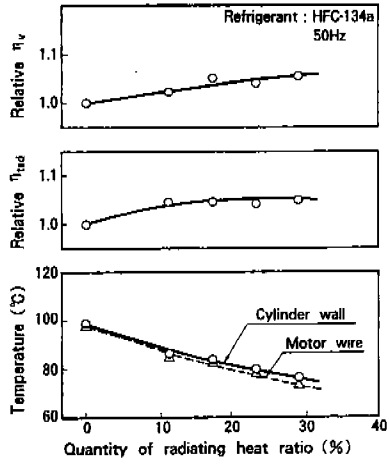

Fig. 9 Performance and temperature versus quantity of radiating heat

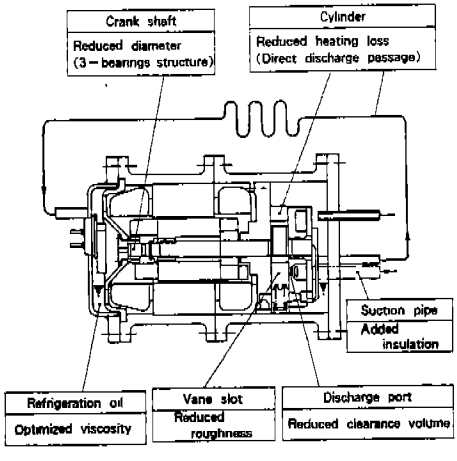

Fig. 10 Structure of prototype compressor

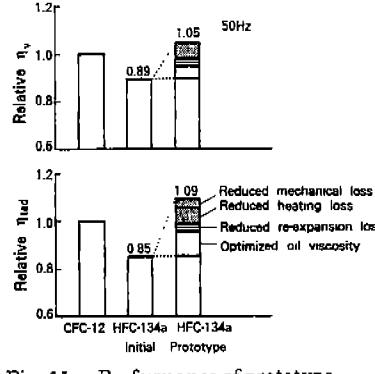

Fig. 11 Performance of prototype compressor

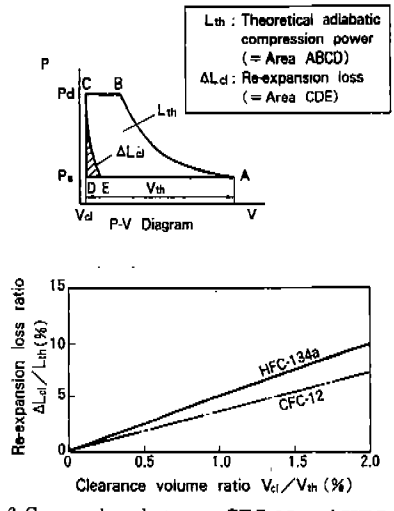

Fig. 6 Comparison between CFC-12 and HFC-134a re-expansion loss

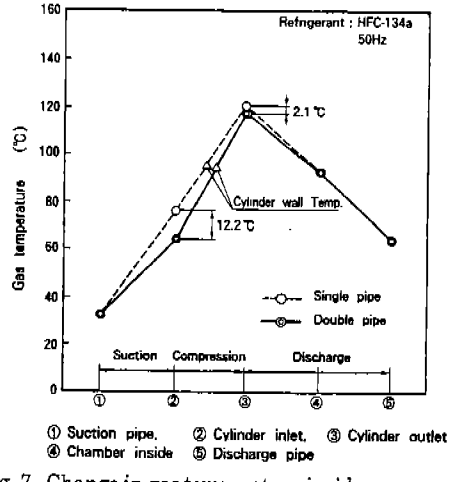

Fig. 7 Change in gas temperature inside compressor

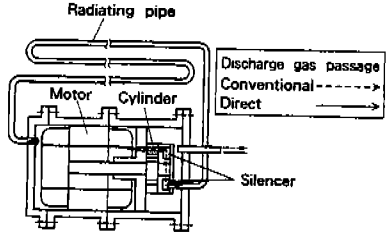

Fig. 8 Passage of discharge gas

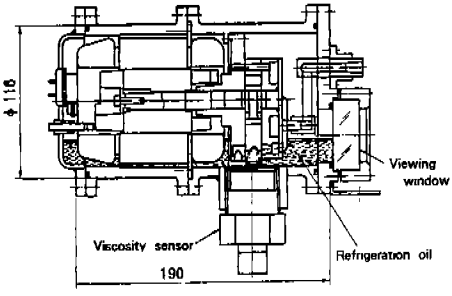

Fig. 3 Structure of compressor for measuring viscosity of HFC-134a / oil mixture

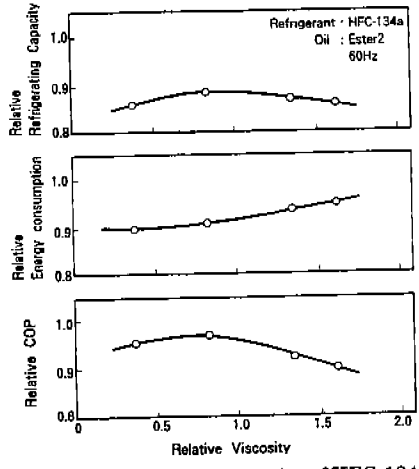

Fig. 4 Performance versus viscosity of HFC-134a / oil mixture (relative to CFC-12 / alkylbenzen oil mixture)

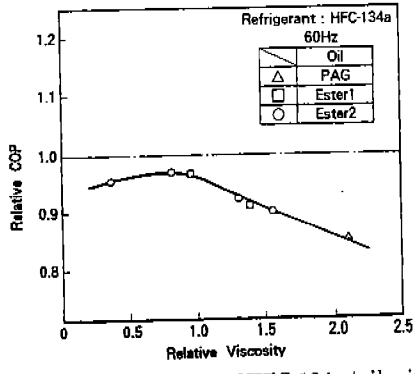

Fig. 5 COP versus viscosity of HFC-134a / oil mixture (relative to CFC-12 / alkylbenzen oil mixture)

viscosity sensor, and by reducing heating loss during compression with the direct discharge passage which decreases the temperature of the cylinder.

Using these methods, we have developed a high efficiency HFC-134a rotary compressor, whose η_{tad} is 9% higher than that of the present CFC-12 one.

REFERENCES

[1] E. A. Vineyard, et al. , "Refrigerator-Freezer Energy Testing with Alternative Refrigerants" , ASHRAE Trans. , Vol. 95, Part 2, 295(1989)
[2] J. L. Boot, "Overview of alternatives to CFCs for domestic refrigerators and freezers" , Int. J. Refrig. , Vol. 13, March, 100(1990)
[3] D. P. Wilson and R. S. Basu, "Thermodynamic properties of a new stratosperically safe working fluid-refrigerant 134a" , ASHRAE Trans. , Vol. 94, Part 2.
[4] K. Kousokabe, et al. , Proc. of the 25th Japanese Joint Conference on Air-conditioning and Refrigeration, 89(1991) (in Japanese)

Table 1 Refrigerant properties of CFC-12 and HFC-134a

	CFC-12	HFC-134a
Suction pressure (MPa)	0.984	1.043
Discharge pressure (MPa)	0.111	0.095
Pressure ratio (−)	8.86	11.01
COP (−)	2.92	2.91
Relative Capacity (−)	1.0	0.92

Condition : − 27.6 ℃ evaporating temp.
32 ℃ compressor suction temp.
41 ℃ condensing temp.
32 ℃ expansion temp.

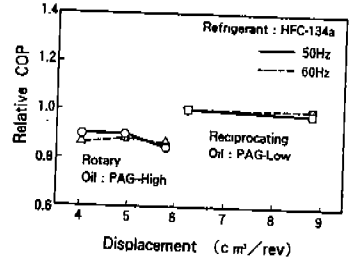

Fig. 1 Performance of compressor using HFC-134a (relative to CFC-12)

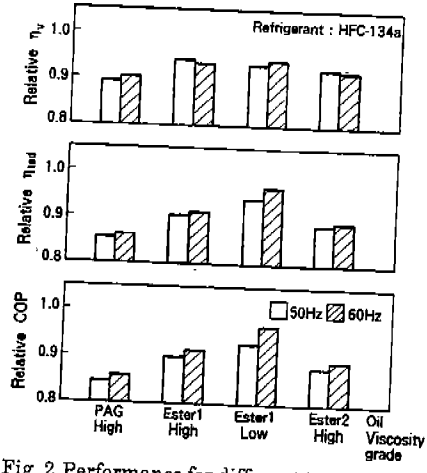

Fig. 2 Performance for different types of oil (relative to CFC-12)

in temperature between the suction gas and the cylinder wall is larger and the suction gas is more subject to heating. This increases indicated work and reduces indicated efficiency. Therefore, to obtain a large increase in η_{tad}, we should lower the temperature of the cylinder itself and reduce the quantity of heat transferred to the suction gas.

As Fig. 8 shows, in the present compressor, the high temperature gas discharged from a cylinder goes through the silencer next to the cylinder and is led to the motor side. As a result, the cylinder is heated. During suction, the low temperature suction gas is heated and expanded, thus η_v decreases. At the early stage of the compression process, as previously described, the gas receives heat from the cylinder wall and indicated work becomes large and indicated efficiency decreases. Therefore, as shown in Fig. 8, we chose a direct discharge passage which decreases the quantity of heat transferred to the cylinder. The high temperature discharge gas is led directly to the outside of the chamber. Then it is cooled by passing it through the radiating pipe and is returned to the inside of the chamber. With the change in length of the radiating pipes, we examined the performance versus the quantity of radiating heat (see Fig. 9). The quantity of radiating heat is represented as the percentage of the consumption energy. As shown in this figure, as the quantity of radiating heat increases, the temperature of the cylinder wall and motor wire decreases and η_v increases significantly. η_{tad} also increases significantly but it has a saturation point. Since in the study of refrigeration oil, HFC-134a / oil mixture viscosity increased as the temperature decreased, η_{tad} is likely to be influenced by the increasing viscosity of the mixture. This method increases η_v by 4% and η_{tad} by 5% for a temperature decrease of 15°C.

PERFORMANCE OF PROTOTYPE COMPRESSOR USING HFC-134a

Structure

We constructed a prototype compressor incorporating all of the improvements described above; namely, optimized oil viscosity, reduced clearance volume at discharge port, reduced crankshaft diameter, reduced vane slot roughness, insulated suction pipe, and added direct discharge passage. The structure of this prototype is shown in Fig. 10.

Performance

The performance of the prototype compressor is shown in Fig. 11, compared with the present compressor using CFC-12 and the initial test using HFC-134a. η_{tad} of the prototype compressor is 9% higher than that of the present compressor using CFC-12. This is a 24% increase over the initial test and is close to the sum of performance increases expected from each improvement. Although it is difficult to distinguish individual contributions, they are probably; 43% by optimized oil viscosity, 15% by reduced clearance volume, that is, reduced re-expansion loss, 27% by reduced heating loss, and 15% by reduced mechanical loss.

The η_v of the prototype compressor is 5% higher than that of the present one. This results from the optimized oil viscosity, reduced clearance volume, and reduced heating loss.

CONCLUSION

When HFC-134a is substituted for CFC-12 in a rotary compressor, the performance decreases. The main causes of this performance decrease are the higher viscosity of the HFC-134a / oil mixture, and the greater re-expansion loss of gas in clearance volume.

The performance can be improved by optimizing the oil viscosity by directly measuring the viscosity of the HFC-134a / oil mixture inside the compressor chamber with a

EFFECT OF RE-EXPANSION LOSS ON PERFORMANCE

Another factor causing the drop in COP is the greater re-expansion loss of gas in clearance volume V_{cl}. Replacing CFC-12 with HFC-134a increases the compression ratio Π ($=P_d/P_s$) by 24% and reduces the adiabatic exponent κ from 1.14 to 1.12. This results in an increase in the re-expansion loss ΔL_{cl}.

$$\Delta Lcl = Ps \cdot Vcl \left[\Pi^{\frac{1}{\kappa}} \frac{\kappa}{\kappa-1} \left(\Pi^{\frac{\kappa-1}{\kappa}} - 1\right) - \Pi + 1\right] \quad \cdots\cdots\cdots\cdots \quad (1)$$

In the theoretical pressure-volume diagram in Fig. 6, the shaded part represents the re-expansion loss. The re-expansion loss for HFC-134a is 34% higher than for CFC-12 at the same clearance volume ratio. Thus the decrease in η_{tad} due to the difference in re-expansion loss is estimated to be about 2% for the measured compressor with the clearance volume ratio of 1.5%.

To avoid a drop in COP or η_{tad}, we must reduce the clearance volume such as discharge port volume. This will also increase η_v because of the increase in theoretical volumetric efficiency.

HIGHER EFFICIENCY COMPRESSOR

We investigated ways to reduce mechanical and heating losses.

Reduction of mechanical loss

We reduced the diameter of the crankshaft to reduce the friction loss at the bearings. The bending induced by this was reduced by adding a supplementary bearing to the end of the motor rotor. Calculations show that the load on the supplementary bearing is much smaller than on the other two bearings, so the increase in friction loss due to the supplementary bearing is negligible.

The roughness of a vane slot was halved to reduce the friction loss at the sides of a vane.

These two reductions of mechanical loss led to an estimated 3% increase in η_{tad}.

Reduction of heating loss

Since the flow rate of refrigerant in a domestic refrigerator is much smaller than that in an air-conditioner, the refrigerant gas in a refrigerator compressor is affected more by heating. First, the suction pipe was insulated. After the gas in the suction pipe enters the chamber of a compressor, the low temperature gas is heated through the suction pipe wall by the high temperature discharge gas inside the chamber. Thus the specific volume of the suction gas becomes large and η_v decreases. Consequently, η_{tad} also decreases. Therefore, to reduce the heating loss of suction gas, we used a double suction pipe with an insulating layer between the two pipes, instead of a single pipe. Experiments showed that the double suction pipe increases η_v by 2% and η_{tad} by 0.7%. The increase of η_{tad} is rather small, compared with that of η_v.

Fig. 7 shows the change in gas temperature inside the compressor. For the double pipe, the gas temperature at the cylinder inlet decreases by 12°C, compared to that for the single pipe, but the gas temperature at the cylinder outlet only decreases by 2°C. The gas temperatures inside the chamber and at the discharge pipe are almost the same. This result suggests that the reason the double suction pipe only produces a small increase in η_{tad}, compared to the large increase in η_v, may be as follows. With the double pipe, the difference

usually used for rotary compressors, whose chamber is filled with high pressure gas, and low VG oil is used for reciprocating compressors, whose chamber is filled with low pressure gas. In this test, the same selection was applied.

Three rotary compressors and two reciprocating compressors with different displacements were tested. The results (see Fig. 1) show that the COP of the reciprocating compressors using HFC-134a is almost the same as for CFC-12, but is 10 - 15% lower for rotary compressors.

Therefore, we investigated the causes of the decrease in performance of rotary compressors using HFC-134a [4].

EFFECT OF REFRIGERATION OIL ON PERFORMANCE

Different oil types

The performances of rotary compressors using different types of oil are shown in Fig. 2. PAG, ester 1, and ester 2 oil with a high VG were compared for a compressor with 5.8 cm^3/rev displacement. To examine the effect of different viscosity grade on performance, ester 1 oil with a low VG was also tested. With PAG oil, volumetric efficiency η_v and total adiabatic efficiency η_{tad} decreased by 11% and 15% respectively. The compressor using ester 1 oil with a high VG had a 3% higher η_v and a 5% higher η_{tad} than a compressor using PAG oil. The ester 1 with a low VG showed a similar η_v to the high VG ester 1, but a 12% higher η_{tad} than the PAG oil. The COP for low VG ester 1 oil also showed a 12% increase. The ester 2 showed a 1% higher η_v and a 3% higher η_{tad} than the PAG.

The cause of the difference in performance of compressors using different types of oil may be the difference in lubricity of each oil, but the difference in oil viscosity is more likely to have great effect on performance from the results for ester 1 oil with a high VG and a low VG.

Different oil viscosity

The viscosity of the HFC-134a / oil mixture is the key factor that influences the compressor performance. The viscosity of the mixture was measured inside the compressor chamber during operation by attaching a viscosity sensor to the compressor (see Fig. 3). In this sensor, the viscosity is determined from the velocity of an object which moves in a fluid. Ester 2 oils having four different VG were used. As shown in Fig. 4, there is an optimum viscosity that maximizes COP. Refrigerating capacity has a maximum. On the other hand, energy consumption decreases, as the viscosity decreases in the measured range. The optimum viscosity for COP is rather smaller than the viscosity of the present CFC-12 / alkylbenzen oil mixture. There are two reasons for the existence of the optimum viscosity for COP. First, with regard to mechanical loss, there is an optimum viscosity that minimizes the friction loss at bearings. Second, the compression chamber of a rotary compressor is sealed with leak-in oil through clearance and the quantity of leak-in oil depends on the viscosity of refrigerant / oil mixture, so there is an optimum quantity of leak-in oil that is adequate for sealing.

Fig. 5 shows COP versus viscosity of HFC-134a / oil mixtures, including the results of other types of oil described before. The results for all types of oil are almost on a line and the effect of different types of oil on performance is small.

This optimization of oil viscosity reduced the drop in COP of the compressor using HFC-134a from -15% to -3%.

DEVELOPMENT OF HIGH EFFICIENCY ROTARY COMPRESSOR FOR DOMESTIC REFRIGERATOR USING HFC-134a

Hirokatsu Kosokabe, Kazuhiro Endoh
Mechanical Engineering Research Laboratory, Hitachi, Ltd.,
Ibaraki, Japan

Hiroshi Iwata, Dr., Hiroaki Hata
Tochigi Works, Hitachi, Ltd., Tochigi, Japan

Mitsuru Fujiwara, Dr.
Muroran Institute of Technology, Hokkaido, Japan

ABSTRACT

In response to the trend for phasing out CFCs, we have developed a high efficiency HFC-134a rotary compressor, whose total adiabatic efficiency is 9% higher than that of the present CFC-12 one. This paper describes the causes for the usual poor performance of rotary compressors using HFC-134a and explains how we improved the performance.

INTRODUCTION

CFCs will be phased out in the mid 1990s. Since CFC-12 is the usual refrigerant for domestic refrigerators, alternative refrigerants urgently need to be developed. The most promising alternative seems to be HFC-134a. However, it has been reported that when HFC-134a is substituted for CFC-12, the performance of refrigerators and compressors decreases [1,2]. Our initial test of rotary compressors using HFC-134a also showed a large drop in performance. Therefore, we investigated the causes of the decrease in performance and developed ways to improve performance. As a result, we have developed a high efficiency rotary compressor using HFC-134a.

HFC-134a REFRIGERANT PROPERTIES

The refrigerant properties of CFC-12 and HFC-134a are compared in Table 1 for the same temperature [3]. Since HFC-134a has a lower suction pressure and a higher discharge pressure than CFC-12, the pressure ratio of HFC-134a is 24% higher than that of CFC-12. The theoretical coefficient of performance (COP) on the Mollier chart of HFC-134a is similar to that of CFC-12 and this indicates no drop in efficiency using HFC-134a. On the other hand, the refrigerating capacity of HFC-134a is 8% smaller than that of CFC-12 and compressors using HFC-134a need a larger displacement to maintain the same capacity.

INITIAL TEST

Since HFC-134a is not compatible with the mineral oil or alkylbenzen oil used with CFC-12, it needs a new oil such as polyalkylene glycol (PAG) oil or ester oil. For the initial test, we used HFC-134a and PAG oil for a compressor calorimeter test using the rotary and reciprocating compressors designed for CFC-12. For CFC-12, high viscosity grade (VG) oil is

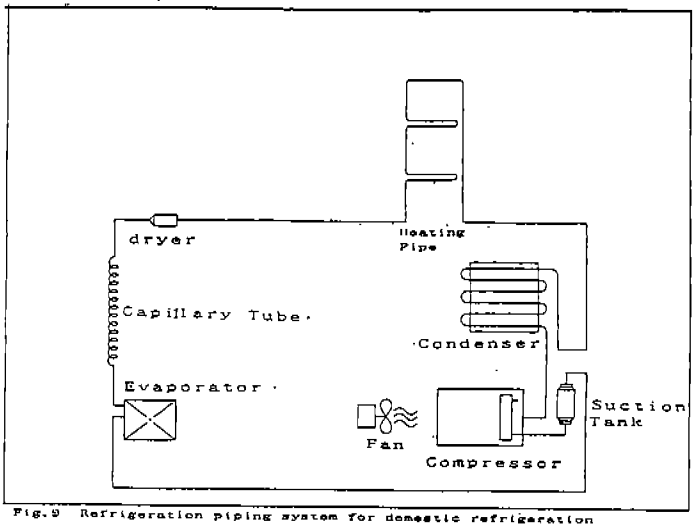

Fig.9 Refrigeration piping system for domestic refrigeration

Table 6 Reliability test of refrigerator using Rotary type compressors

Refrigerant		CFC12	HFC134a							
oil		AB	E2	E3	E6		E7		
additive		—	—	stabilizerA	stabilizerA		stabilizerC		
motor coil temp. (℃)		125	125	125	125	135	125	135	143
test time (days)		90	30 Stopped	90	90	90	90	90	90
result	refrigeration capacity	OK	NOT OK	OK	OK	OK	OK	OK	OK
	refrigerant	OK	NOT OK	OK	OK	OK	OK	OK	OK
	oil	OK	NOT OK (large AV)	NOT OK (large AV)	OK	OK	OK	OK	OK
	motor materials	OK	OK	OK	OK	OK	OK	OK	OK
	molecular sieves	OK	OK	OK	OK	OK	OK	OK	OK
	piping parts	OK	NOT OK metal soap	NOT OK metal soap	OK	OK	OK	OK	OK
	sliding parts of compressor	OK	Corrosion wear	Corrosion wear	OK	OK	OK	OK	OK
	Total	OK	NOT OK	NOT OK	OK	OK	OK	OK	OK